Young asteroid families as the primary source of meteorites

M. Brož[1], P. Vernazza[2], M. Marsset[3,4], F.E. DeMeo[4], R.P. Binzel[4], D. Vokrouhlický[1], D. Nesvorný[5]

[1] *Charles University, Faculty of Mathemtics and Physics, Institute of Astronomy, V Holešovičkách 2, 18000 Prague 8, Czech Republic*

[2] *Aix Marseille University, CNRS, CNES, LAM, Institut Origines, Marseille, France*

[3] *European Southern Observatory (ESO), Alonso de Cordova 3107, 1900 Casilla Vitacura, Santiago, Chile*

[4] *Department of Earth, Atmospheric and Planetary Sciences, MIT, 77 Massachusetts Avenue, Cambridge, MA 02139, USA*

[5] *Department of Space Studies, Southwest Research Institute, 1050 Walnut Street, Suite 300, Boulder, CO 80302, USA*

Understanding the origin of bright shooting stars and their meteorite samples is among the most ancient astronomy-related questions that at larger scales has human consequences [1–3]. As of today, only $\sim 6\%$ of meteorite falls have been firmly linked to their sources (Moon, Mars, and asteroid (4) Vesta; [4–6]). Here, we show that $\sim 70\%$ of meteorites originate from three recent breakups of $D > 30\,\mathrm{km}$ asteroids that occurred 5.8, 7.5 and less than ~ 40 million years ago. These breakups, including the well-known Karin family [7], took place in the prominent yet old Koronis and Massalia families and are at the origin of the dominance of H and L ordinary chondrites among meteorite falls. These young families distinguish themselves amidst all main belt asteroids by having a uniquely high abundance of small fragments. Their size-frequency distribution remains steep for a few tens of millions of years,

exceeding temporarily the production of metre-sized fragments by the largest old asteroid families (e.g., Flora, Vesta). Supporting evidence includes the existence of associated dust bands [8–10], the cosmic-ray exposure ages of H-chondrite meteorites [11,12], or the distribution of pre-atmospheric orbits of meteorites [13–15].

According to both dynamical models [16–18] and observational surveys [19–21], the majority of meteorites are thought to have their origin in the main asteroid belt. However, it is exceedingly challenging to determine the provenance of the different meteorite groups (e.g., H, L, LL, CM) using current telescopic and spacecraft data alone, as plausible parent bodies or parent families are not spectrally/compositionally unique (e.g., [22–25]). (4) Vesta and its family stand out as an obvious exception, being the only possible source of HEDs [4]. Identifying the sources of the main meteorite groups thus remains an unresolved problem in planetary science. Notably, meteorite falls are dominated by two groups only (H and L chondrites) that represent $\sim 70\%$ of all falls; they are followed at significantly less proportion by LL chondrites (8%) and HEDs (6%). On the contrary, kilometre-sized asteroids in the main belt, as well as near-Earth objects (NEOs), typically have a different composition, with LL-like bodies being as abundant as H- or L-like bodies [20,24]. Specifically, the Flora (LL) and Vesta (HED) families comprise the largest numbers of kilometre-sized asteroids among all H-, L-, LL- and HED-like families (SI Fig. 5). Consequently, neither the background population nor prominent asteroid families are likely significant sources of the meteorite flux.

Instead, a few recent stochastic collisional events may be the main source of the meteorite flux, as suggested by the cosmic-ray exposure (CRE) ages [11]. About 40% of all H chondrites have young CRE ages in the 5-8 My range, indicating a recent breakup of an H-chondrite-like body. The Karin family, a part of the Koronis family, is the only known H-chondrite-like family with a formation age in the 5-8 My range (5.8 My, [7]). Whereas it may explain some part of the CRE distribution it can hardly explain the older and more abundant 7-8 My ages.

To constrain the main source of H chondrites, we searched for additional and relatively young S-type families across the main belt and, in particular, among all major H-like families (Agnia, Koronis, Maria, Merxia, Phocaea). We identified three clusters, all in the Koronis family (Fig. 1). Out of the three clusters, only the Koronis$_2$ family [26], exhibits a convergence of orbits at the corresponding age of $(7.5 \pm 0.1)\,\mathrm{My}$ (Fig. 2; SI). Among the young Koronis families, Koronis$_2$ has the steepest size-frequency distribution (SFD; with the power-law slope -4.0), followed by Karin (-2.9). When extrapolated to small sizes, the SFD of Karin 'overlays' the prominent 2.1-degree IRAS dust band [27] (Fig. 3). This strongly supports a continuous SFD from large (sub-km) fragments, to intermediate metre-sized bodies (i.e., precursor bodies of meteorites), and to very small (100-$\mu\mathrm{m}$) dust particles. Both Karin and Koronis$_2$ have exactly the same inclination as the 2.1-degree IRAS dust band and it is therefore likely that the two families are at its origin. Notably, Koronis$_2$ should dominate Karin already at sub-km sizes. When interpolated, the two SFDs amount to a substantial number of metre-sized bodies, 30-60×10^{10} (Karin) and 100-300×10^{10} (Koronis$_2$).

To determine whether this number of metre-sized bodies overcomes that of the largest S-type families (Agnia, Eunomia, Flora, Gefion, Juno, Koronis, Massalia, Maria, Merxia, Nysa, Phocaea; SI Fig. 6), we used a collisional model — specifically, a Monte-Carlo statistical approach (Boulder; ref. [28]) — to extrapolate their observed SFDs down to $D = 1\,\mathrm{m}$. This extrapolation is not trivial, because the respective slope for $D < 1\,\mathrm{km}$ is not constant due to interactions with the main belt population [15,29,30]. For each family, the model must be set up individually, because each of them has a different age. Consequently, both the main belt's and the family's initial SFDs must be adapted, so that the final SFD corresponds to the observations, which are complete for $D \gtrsim 1\,\mathrm{km}$. Every model was run at least 10 times to determine its uncertainties, which are mostly due to the stochasticity of collisions (see SI for more details). Next, we used an orbital model [31] to determine the decay time scales $\tau_{\rm mb}$ of families in the main belt and the mean lifetimes $\bar{\tau}_{\rm neo}$ of bodies that escaped as NEOs. Our N-body model is based on a symplectic integrator (SWIFT; ref. [32]). It takes into account a number of effects driving the transport, in particular, perturbations by 11 massive bodies (Sun, Mercury to Neptune, Ceres, Vesta), gravitational resonances, close encounters, the Yarkovsky effect [33–35], the YORP effect [36], collisional reorientations, and size-dependent spin limits (see SI for more details). We computed approximately 10^3 mass-less particles per family (and per size D), allowing us to estimate steady-state NEO populations as $N_{\rm neo}(>D) = N_{\rm mb}(>D)\bar{\tau}_{\rm neo}/\tau_{\rm mb}$.

We find that the Karin and Koronis$_2$ families are far more productive in terms of meteoroids (by at least a factor of 10) than any of the largest families (Figs. 3, 4). When the Karin and Koronis$_2$ metre-sized bodies are transported from the main belt to the NEO space, their numbers are relatively decreased due to their unfavourably short NEO lifetimes. Nevertheless, their abundance is still greater than the total number of metre-sized NEOs originating from the Vesta and Flora families, in agreement with meteorite falls statistics.

To have a better understanding of the physical process at play, we ran our collisional evolution model with an initially steep Karin-like SFD (-2.9) and let it evolve for up to $100\,\mathrm{My}$. After

100 My of collisional evolution (Fig. 3), the slope of the SFD at sub-km sizes already becomes much shallower (-1.4) and the number of metre-sized bodies within the family is already less important than in the Vesta or Flora families. This explains for example today's minimal contribution of the 100 My-old Agnia family to the current meteorite flux. It follows that only recent ($\lesssim 40\,\mathrm{My}$) yet sufficiently large ($D > 30\,\mathrm{km}$) breakups can overcome the meteorite production originating from the largest old families.

Overall, our numerical simulations produce relative abundances of H-, L-, LL- and HED-like bodies (Fig. 4) that are in excellent agreement (within 10%) with the compositional distribution of NEOs [21] and the meteorite fall statistics [37]. For kilometre-sized NEOs, the Phocaea, Juno and Flora families are by far the main sources of H-, L- and LL-like NEOs, respectively. At metre sizes, the Karin (H), Koronis$_2$ (H), Massalia$_2$ (L) and Flora (LL) families are by far the main sources of H-, L- and LL-like meteorites. This is well supported by the pre-atmospheric orbits of meteorites [13,14,38]. As demonstrated in SI Fig. 20, some H chondrites with the semimajor axis 2.5-$2.8\,\mathrm{au}$ and low inclination ($\lesssim 3°$) directly point to the Karin and Koronis families.

There are two other major events with associated prominent dust bands, namely $\sim 40\,\mathrm{My}$ ago in Massalia (L-like; ref. [39]) and 8.3 My ago in Veritas (CM-like; [10,25,40]) families. Using similar arguments as above, they should therefore be major sources of L-like (as discussed in ref. [39]) and also CM-like metre-sized fragments, implying that the total meteorite flux is largely dominated by only four recent ($\lesssim 40\,\mathrm{My}$) collisional events. Notably, CM-like meteoroids originating from the Veritas family should be so common (~ 3 times more than H chondrites) that the Earth should experience an 'extraterrestrial rain' of CM-like material of the same order ($10^{-6}\,\mathrm{km}^{-2}\,\mathrm{y}^{-1}$;

cf. SI Tab. 11) as the total meteorite flux [41]. It follows that the bias due to atmospheric entry for the friable CM chondrites (1.5% of the falls) amounts to a factor of ~ 40 with respect to the consolidated ordinary chondrites, highlighting the critical need of sample return missions [42,43] for the minute study of highly fragile extraterrestrial materials.

Data availability The initial conditions of simulations and data used to produce the figures are available at `http://sirrah.troja.mff.cuni.cz/~mira/hchondrites/`.

Code availability The collisional code is available at the previous URL.

1. Chladni, E. F. F. *Über den Ursprung der von Pallas Gefundenen und anderer ihr ähnlicher Eisenmassen, und Über Einige Damit in Verbindung stehende Naturerscheinungen* (Johan Friedrich Hartknoch, Riga, 1794).

2. Biot, J.-B. Vorläufige Nachricht von dem Steinregen zu l'Aigle, am 26sten April 1803. *Annalen der Physik* **15**, 74–76 (1803).

3. Kulik, L. A. Otčet meteoritičeskoj ekspedicii o rabotach proizvedennych s 19 Maja 1921 g. po 29 Nojabrja 1922 g. *Izvestija Rossijskoj Akademii Nauk* **16**, 391–410 (1922). URL `https://tunguska.tsc.ru/ru/science/bib/1920-29/1922/1/`.

4. Marvin, U. B. The discovery and initial characterization of Allan Hills 81005: The first lunar meteorite. *Geophys. Res. Let.* **10**, 775–778 (1983).

5. Treiman, A. H., Gleason, J. D. & Bogard, D. D. The SNC meteorites are from Mars. *Planet. Space Sci.* **48**, 1213–1230 (2000).

6. Thomas, P. C. *et al.* Impact excavation on asteroid 4 Vesta: Hubble Space Telescope results. *Science* **277**, 1492–1495 (1997).

7. Nesvorný, D., Bottke, J., William F., Dones, L. & Levison, H. F. The recent breakup of an asteroid in the main-belt region. *Nature* **417**, 720–771 (2002).

8. Sykes, M. V. Zodiacal dust bands: Their relation to asteroid families. *Icarus* **85**, 267–289 (1990).

9. Reach, W. T., Franz, B. A. & Weiland, J. L. The Three-Dimensional Structure of the Zodiacal Dust Bands. *Icarus* **127**, 461–484 (1997).

10. Nesvorný, D., Bottke, W. F., Levison, H. F. & Dones, L. Recent Origin of the Solar System Dust Bands. *Astrophys. J.* **591**, 486–497 (2003).

11. Graf, T. & Marti, K. Collisional history of H chondrites. *J. Geophys. Res.* **100**, 21247–21264 (1995).

12. Eugster, O., Herzog, G. F., Marti, K. & Caffee, M. W. Irradiation Records, Cosmic-Ray Exposure Ages, and Transfer Times of Meteorites. In Lauretta, D. S. & McSween, H. Y. (eds.) *Meteorites and the Early Solar System II*, 829 (Univ. Arizona Press, 2006).

13. Spurný, P., Borovička, J. & Shrbený, L. The Žďár nad Sázavou meteorite fall: Fireball trajectory, photometry, dynamics, fragmentation, orbit, and meteorite recovery. *Met. Planet. Sci.* **55**, 376–401 (2020). `1912.11784`.

14. Brown, P., Wiegert, P., Clark, D. & Tagliaferri, E. Orbital and physical characteristics of meter-scale impactors from airburst observations. *Icarus* **266**, 96–111 (2016). `1511.07479`.

15. Jenniskens, P. *et al.* CAMS newly detected meteor showers and the sporadic background. *Icarus* **266**, 384–409 (2016).

16. Bottke, W. F. *et al.* Debiased Orbital and Absolute Magnitude Distribution of the Near-Earth Objects. *Icarus* **156**, 399–433 (2002).

17. Granvik, M. *et al.* Debiased orbit and absolute-magnitude distributions for near-Earth objects. *Icarus* **312**, 181–207 (2018). 1804.10265.

18. Nesvorný, D. *et al.* NEOMOD: A New Orbital Distribution Model for Near Earth Objects. *arXiv e-prints* arXiv:2306.09521 (2023). 2306.09521.

19. Binzel, R. P., Bus, S. J., Burbine, T. H. & Sunshine, J. M. Spectral Properties of Near-Earth Asteroids: Evidence for Sources of Ordinary Chondrite Meteorites. *Science* **273**, 946–948 (1996).

20. Vernazza, P. *et al.* Compositional differences between meteorites and near-Earth asteroids. *Nature* **454**, 858–860 (2008).

21. Marsset, M. *et al.* The Debiased Compositional Distribution of MITHNEOS: Global Match between the Near-Earth and Main-belt Asteroid Populations, and Excess of D-type Near-Earth Objects. *Astron. J.* **163**, 165 (2022). 2202.13796.

22. Bus, S. J. & Binzel, R. P. Phase II of the Small Main-Belt Asteroid Spectroscopic Survey. A Feature-Based Taxonomy. *Icarus* **158**, 146–177 (2002).

23. DeMeo, F. E., Binzel, R. P., Slivan, S. M. & Bus, S. J. An extension of the Bus asteroid taxonomy into the near-infrared. *Icarus* **202**, 160–180 (2009).

24. Vernazza, P. *et al.* Multiple and Fast: The Accretion of Ordinary Chondrite Parent Bodies. *Astrophys. J.* **791**, 120 (2014). 1405.6850.

25. Vernazza, P. *et al.* Compositional Homogeneity of CM Parent Bodies. *Astron. J.* **152**, 54 (2016).

26. Molnar, L. A. & Haegert, M. J. Details of Recent Collisions of Asteroids 832 Karin and 158 Koronis. In *AAS/Division for Planetary Sciences Meeting Abstracts #41*, vol. 41 of *AAS/Division for Planetary Sciences Meeting Abstracts*, 27.05 (2009).

27. Nesvorný, D., Vokrouhlický, D., Bottke, W. F. & Sykes, M. Physical properties of asteroid dust bands and their sources. *Icarus* **181**, 107–144 (2006).

28. Morbidelli, A., Bottke, W. F., Nesvorný, D. & Levison, H. F. Asteroids were born big. *Icarus* **204**, 558–573 (2009). 0907.2512.

29. Campo Bagatin, A., Cellino, A., Davis, D. R., Farinella, P. & Paolicchi, P. Wavy size distributions for collisional systems with a small-size cutoff. *Planet. Space Sci.* **42**, 1079–1092 (1994).

30. O'Brien, D. P. & Greenberg, R. The collisional and dynamical evolution of the main-belt and NEA size distributions. *Icarus* **178**, 179–212 (2005).

31. Brož, M., Vokrouhlický, D., Morbidelli, A., Nesvorný, D. & Bottke, W. F. Did the Hilda collisional family form during the late heavy bombardment? *Mon. Not. R. Astron. Soc.* **414**, 2716–2727 (2011). 1109.1114.

32. Levison, H. F. & Duncan, M. J. The long-term dynamical behavior of short-period comets. *Icarus* **108**, 18–36 (1994).

33. Yarkovsky, I. O. *Plotnosť svetovogo efira i okazyvaemoe im soprotivlenie dviženiu* (Typografia Judina, Bryansk, 1901).

34. Vokrouhlický, D. Diurnal Yarkovsky effect as a source of mobility of meter-sized asteroidal fragments. I. Linear theory. *Astron. Astrophys.* **335**, 1093–1100 (1998).

35. Vokrouhlický, D. & Farinella, P. The Yarkovsky Seasonal Effect on Asteroidal Fragments: A Nonlinearized Theory for Spherical Bodies. *Astron. J.* **118**, 3049–3060 (1999).

36. Čapek, D. & Vokrouhlický, D. The YORP effect with finite thermal conductivity. *Icarus* **172**, 526–536 (2004).

37. Gattacceca, J. *et al.* The Meteoritical Bulletin, No. 110. *Met. Planet. Sci.* **57**, 2102–2105 (2022).

38. Meier, M. Meteorite Orbits (2023). URL `https://www.meteoriteorbits.info/`.

39. Marsset, M. *et al.* The Massalia asteroid family as the origin of ordinary L chondrites. *Nature* (submit.).

40. Farley, K. A., Vokrouhlický, D., Bottke, W. F. & Nesvorný, D. A late Miocene dust shower from the break-up of an asteroid in the main belt. *Nature* **439**, 295–297 (2006).

41. Ceplecha, Z. Influx of interplanetary bodies onto earth. *Astron. Astrophys.* **263**, 361–366 (1992).

42. Lauretta, D. S. *et al.* The unexpected surface of asteroid (101955) Bennu. *Nature* **568**, 55–60 (2019).

43. Watanabe, S. *et al.* Hayabusa2 arrives at the carbonaceous asteroid 162173 Ryugu—A spinning top-shaped rubble pile. *Science* **364**, 268–272 (2019).

44. Novaković, B., Tsiganis, K. & Knežević, Z. Chaotic transport and chronology of complex asteroid families. *Mon. Not. R. Astron. Soc.* **402**, 1263–1272 (2010). 0910.5857.

45. Bottke, W. F. *et al.* The Collisional Evolution of the Main Asteroid Belt. In Michel, P., DeMeo, F. E. & Bottke, W. F. (eds.) *Asteroids IV*, 701–724 (Univ. Arizona Press, 2015).

46. Moskovitz, N. *et al.* Modernizing Lowell Observatory's astorb Database. In *EPSC-DPS Joint Meeting 2019*, vol. 2019, EPSC–DPS2019–644 (2019).

47. Knežević, Z. & Milani, A. Proper element catalogs and asteroid families. *Astron. Astrophys.* **403**, 1165–1173 (2003).

48. Novaković, B. & Radović, V. Asteroid Families Portal. In *EPSC-DPS Joint Meeting 2019*, vol. 2019, EPSC–DPS2019–1671 (2019).

49. Nugent, C. R. *et al.* NEOWISE Reactivation Mission Year One: Preliminary Asteroid Diameters and Albedos. *Astrophys. J.* **814**, 117 (2015). 1509.02522.

50. Usui, F. *et al.* Asteroid Catalog Using Akari: AKARI/IRC Mid-Infrared Asteroid Survey. *Publ. Astron. Soc. Pacific* **63**, 1117–1138 (2011).

51. Parker, A. *et al.* The size distributions of asteroid families in the SDSS Moving Object Catalog 4. *Icarus* **198**, 138–155 (2008). 0807.3762.

52. Zappalà, V., Bendjoya, P., Cellino, A., Farinella, P. & Froeschlé, C. Asteroid families: Search of a 12,487-asteroid sample using two different clustering techniques. *Icarus* **116**, 291–314 (1995).

53. Vokrouhlický, D., Brož, M., Bottke, W. F., Nesvorný, D. & Morbidelli, A. Yarkovsky/YORP chronology of asteroid families. *Icarus* **182**, 118–142 (2006).

54. Nesvorný, D., Brož, M. & Carruba, V. Identification and Dynamical Properties of Asteroid Families. In Michel, P., DeMeo, F. E. & Bottke, W. F. (eds.) *Asteroids IV*, 297–321 (Univ. Arizona Press, 2015).

55. Vokrouhlický, D., Brož, M., Bottke, W. F., Nesvorný, D. & Morbidelli, A. The peculiar case of the Agnia asteroid family. *Icarus* **183**, 349–361 (2006).

56. Walsh, K. J., Delbó, M., Bottke, W. F., Vokrouhlický, D. & Lauretta, D. S. Introducing the Eulalia and new Polana asteroid families: Re-assessing primitive asteroid families in the inner Main Belt. *Icarus* **225**, 283–297 (2013). 1305.2821.

57. Hendler, N. P. & Malhotra, R. Observational Completion Limit of Minor Planets from the Asteroid Belt to Jupiter Trojans. *Planet. Sci. J.* **1**, 75 (2020). 2010.07822.

58. Benz, W. & Asphaug, E. Catastrophic Disruptions Revisited. *Icarus* **142**, 5–20 (1999). arXiv:astro-ph/9907117.

59. Bottke, W. F. *et al.* Interpreting the Cratering Histories of Bennu, Ryugu, and Other Spacecraft-explored Asteroids. *Astron. J.* **160**, 14 (2020).

60. Vernazza, P. *et al.* The impact crater at the origin of the Julia family detected with VLT/SPHERE? *Astron. Astrophys.* **618**, A154 (2018).

61. Ševeček, P. *et al.* SPH/N-Body simulations of small ($D = 10\,$km) asteroidal breakups and improved parametric relations for Monte-Carlo collisional models. *Icarus* **296**, 239–256 (2017).

62. Harris, A. W. *et al.* Asteroid Impacts and Modern Civilization: Can We Prevent a Catastrophe? In Michel, P., DeMeo, F. E. & Bottke, W. F. (eds.) *Asteroids IV*, 835–854 (Univ. Arizona Press, 2015).

63. O'Brien, D. P. *et al.* Constraining the cratering chronology of Vesta. *Planet. Space Sci.* **103**, 131–142 (2014). 1407.3303.

64. Marchi, S. *et al.* The Violent Collisional History of Asteroid 4 Vesta. *Science* **336**, 690 (2012).

65. Brož, M., Chrenko, O., Nesvorný, D. & Dauphas, N. Early terrestrial planet formation by torque-driven convergent migration of planetary embryos. *Nature Astronomy* **5**, 898–902 (2021). 2109.11385.

66. Marzari, F., Davis, D. & Vanzani, V. Collisional evolution of asteroid families. *Icarus* **113**, 168–187 (1995).

67. Nesvorný, D., Vokrouhlický, D., Morbidelli, A. & Bottke, W. F. Asteroidal source of L chondrite meteorites. *Icarus* **200**, 698–701 (2009).

68. Aljbaae, S., Souchay, J., Prado, A. F. B. A. & Chanut, T. G. G. A dynamical study of the Gefion asteroid family. *Astron. Astrophys.* **622**, A39 (2019).

69. Holsapple, K. A. Spin limits of Solar System bodies: From the small fast-rotators to 2003 EL61. *Icarus* **187**, 500–509 (2007).

70. Quinn, T. R., Tremaine, S. & Duncan, M. A three million year integration of the earth's orbit. *Astron. J.* **101**, 2287–2305 (1991).

71. Šidlichovský, M. & Nesvorný, D. Frequency modified Fourier transform and its applications to asteroids. *Celestial Mechanics and Dynamical Astronomy* **65**, 137–148 (1996).

72. Brož, M. & Morbidelli, A. The Eos family halo. *Icarus* **223**, 844–849 (2013). 1302.1447.

73. Marsset, M. *et al.* The violent collisional history of aqueously evolved (2) Pallas. *Nature Astronomy* **4**, 569–576 (2020).

74. Harris, A. W. & Chodas, P. W. The population of near-earth asteroids revisited and updated. *Icarus* **365**, 114452 (2021).

75. Gradie, J. C., Chapman, C. R. & Tedesco, E. F. Distribution of taxonomic classes and the compositional structure of the asteroid belt. In Binzel, R. P., Gehrels, T. & Matthews, M. S. (eds.) *Asteroids II*, 316–335 (1989).

76. Nesvorný, D. & Bottke, W. F. Detection of the Yarkovsky effect for main-belt asteroids. *Icarus* **170**, 324–342 (2004).

77. Carruba, V., Nesvorný, D. & Vokrouhlický, D. Detection of the YORP Effect for Small Asteroids in the Karin Cluster. *Astron. J.* **151**, 164 (2016). 1603.09612.

78. Vokrouhlický, D., Brož, M., Novaković, B. & Nesvorný, D. The young Hobson family: Possible binary parent body and low-velocity dispersal. *Astron. Astrophys.* **654**, A75 (2021). 2108.05260.

79. Love, S. G. & Brownlee, D. E. A Direct Measurement of the Terrestrial Mass Accretion Rate of Cosmic Dust. *Science* **262**, 550–553 (1993).

80. Nesvorný, D. *et al.* Origin of the Near-Ecliptic Circumsolar Dust Band. *Astrophys. J. Lett.* **679**, L143 (2008).

81. Swindle, T. D., Kring, D. A. & Weirich, J. R. 40Ar/39Ar ages of impacts involving ordinary chondrite meteorites. *Geological Society of London Special Publications* **378**, 333–347 (2014).

82. Bottke, W. F. *et al.* Linking the collisional history of the main asteroid belt to its dynamical excitation and depletion. *Icarus* **179**, 63–94 (2005).

83. Russell, C. T. *et al.* Dawn at Vesta: Testing the Protoplanetary Paradigm. *Science* **336**, 684 (2012).

84. Carry, B. Density of asteroids. *Planet. Space Sci.* **73**, 98–118 (2012). 1203.4336.

85. Durda, D. D. *et al.* Size-frequency distributions of fragments from SPH/ N-body simulations of asteroid impacts: Comparison with observed asteroid families. *Icarus* **186**, 498–516 (2007).

86. Vernazza, P. *et al.* VLT/SPHERE imaging survey of the largest main-belt asteroids: Final results and synthesis. *Astron. Astrophys.* **654**, A56 (2021).

87. Carruba, V. An analysis of the region of the Phocaea dynamical family. *Mon. Not. R. Astron. Soc.* **398**, 1512–1526 (2009).

88. Brož, M. *et al.* Constraining the cometary flux through the asteroid belt during the late heavy bombardment. *Astron. Astrophys.* **551**, A117 (2013). `1301.6221`.

89. Greenwood, R. C., Schmitz, B., Bridges, J. C., Hutchison, R. & Franchi, I. A. Disruption of the L chondrite parent body: New oxygen isotope evidence from Ordovician relict chromite grains. *Earth and Planetary Science Letters* **262**, 204–213 (2007).

90. Carruba, V. & Nesvorný, D. Constraints on the original ejection velocity fields of asteroid families. *Mon. Not. R. Astron. Soc.* **457**, 1332–1338 (2016). `1602.04486`.

91. Vokrouhlický, D., Bottke, W. F. & Nesvorný, D. Forming the Flora Family: Implications for the Near-Earth Asteroid Population and Large Terrestrial Planet Impactors. *Astron. J.* **153**, 172 (2017).

92. Dykhuis, M. J. & Greenberg, R. Collisional family structure within the Nysa-Polana complex. *Icarus* **252**, 199–211 (2015). `1501.04649`.

93. Rubincam, D. P. Radiative Spin-up and Spin-down of Small Asteroids. *Icarus* **148**, 2–11 (2000).

94. Golubov, O. & Krugly, Y. N. Tangential Component of the YORP Effect. *Astrophys. J. Lett.* **752**, L11 (2012). `1408.1640`.

95. Ševeček, P., Brož, M., Čapek, D. & Ďurech, J. The thermal emission from boulders on (25143) Itokawa and general implications for the YORP effect. *Mon. Not. R. Astron. Soc.* **450**, 2104–2115 (2015). `1504.00566`.

96. Greenberg, R. Orbital interactions - A new geometrical formalism. *Astron. J.* **87**, 184–195 (1982).

Acknowledgements This work has been supported by the Czech Science Foundation through grant 21-11058S (M. Brož and D. Vokrouhlický). We thank B. Bottke and M. Granvik for discussions about the subject of this work.

Author Contributions M.B. and P.V. led the research and wrote the manuscript. M.B. computed the collisional and orbital simulations. M.M., P.V., F.D., R.B. provided and analyzed the spectroscopic observations. D.V., D.N. interpreted the simulations.

Competing Interests The authors declare that they have no competing financial interests.

Correspondence Correspondence and requests for materials should be addressed to M.B. (email: mira@sirrah.troja.mff.cuni.cz).

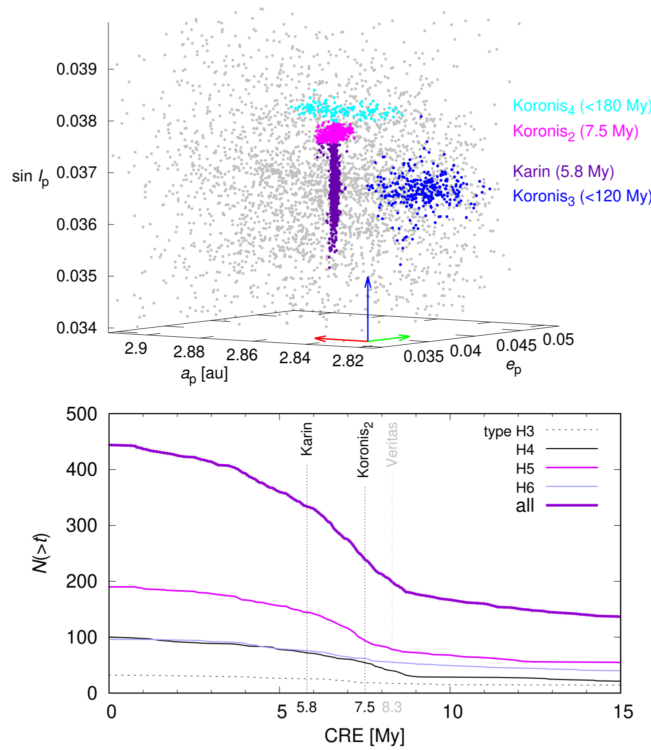

Figure 1: **The Karin and Koronis$_2$ families as the main source of H chondrites.** Top: The space of proper orbital elements $(a_\mathrm{p}, e_\mathrm{p}, \sin I_\mathrm{p})$ viewed from a suitable oblique direction, when the Karin (violet) and the Koronis$_2$ (magenta) families appear as the most compact clusters. Their ages 5.8 and 7.5 My were determined by a convergence of orbits (ref. [7] and this work). Other clusters — provisionally designated Koronis$_3$ (blue) and Koronis$_4$ (cyan) — are much older (possibly up to 120 and 180 My) and extended along the semimajor axis a_p due to the Yarkovsky effect, but they remained compact in the eccentricity e_p and inclination $\sin I_\mathrm{p}$. Bottom: The cumulative distribution of CRE ages of H-chondrite meteorites [11], with contributions of individual types (H3, H4, H5, H6). Most of the meteorites exhibit ages between 5-8 My, which corresponds exactly to the ages of Karin and Koronis$_2$; especially H5. The onset at 8.3 My is close to the age of Veritas [44], which may have induced a collisional cascade in the Koronis family.

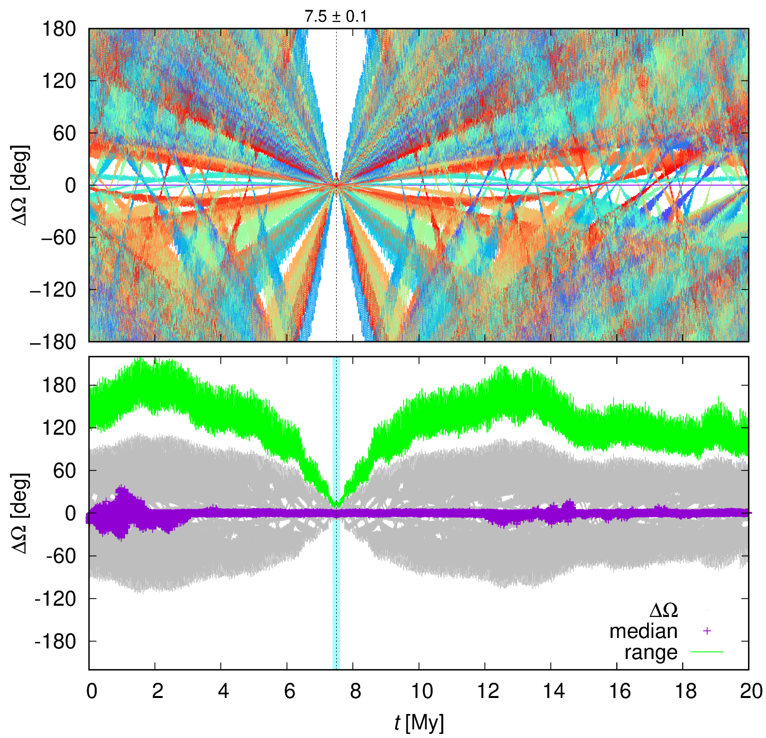

Figure 2: **The Koronis$_2$ family is 7.5 My old from convergence of orbits.** Convergence of the longitude of nodes $\Delta\Omega$ was computed for 100 bodies and 20 clones for each body, in order to include the Yarkovsky effect. Top: a subset of a set of selected clones (colours). Bottom: the clones (gray), the median (violet), and the range (green) of $\Delta\Omega$ distribution. The percentage of interlopers (removed) is up to 50 %, due to contamination from the neighbouring Karin family. The orbits exhibit a clear convergence at $(7.5 \pm 0.1)\,\mathrm{My}$.

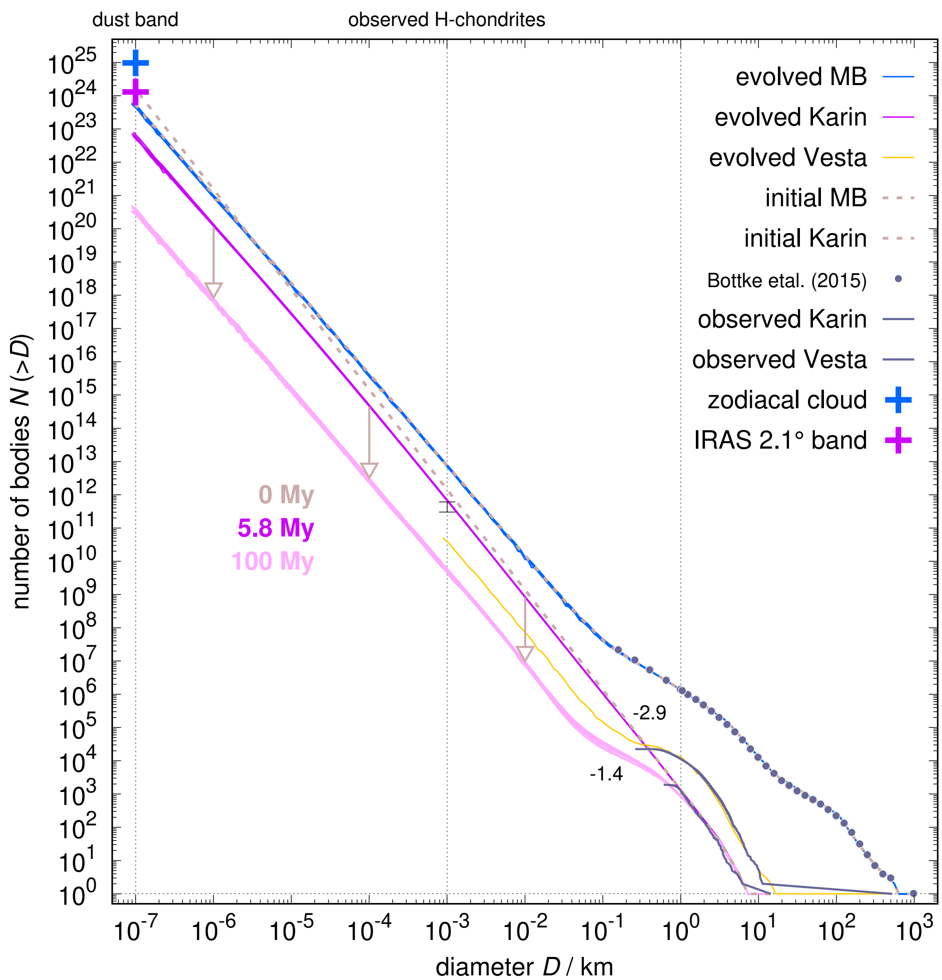

Figure 3: **Excess of metre-sized bodies among young families with respect to large but old ones.** The synthetic SFD of the Karin family (magenta) does not evolve much over the age 5.8 My, as determined by convergence of orbits [7]. The SFD was initially steep ($N(>D) = CD^q$, $q = -2.9$), i.e., close to the observed value at multi-kilometre sizes. After 100 My of collisional evolution, the SFD becomes shallow (-1.4) at sub-km sizes due to interactions with the main belt population (blue; cf. [45]) and the number of metre-sized bodies within young families is already lower than in large and old families such as Vesta and Flora. The observed SFD of the Karin family (gray) is constrained both at multi-kilometre sizes and at $100\,\mu\mathrm{m}$, by observations of the $2.1°$ IRAS dust band. The value of $N(>100\,\mu\mathrm{m}) = 1.3 \times 10^{24}$ particles, is indicated by a cross. The interpolated population of metre-sized bodies is indicated by an error bar.

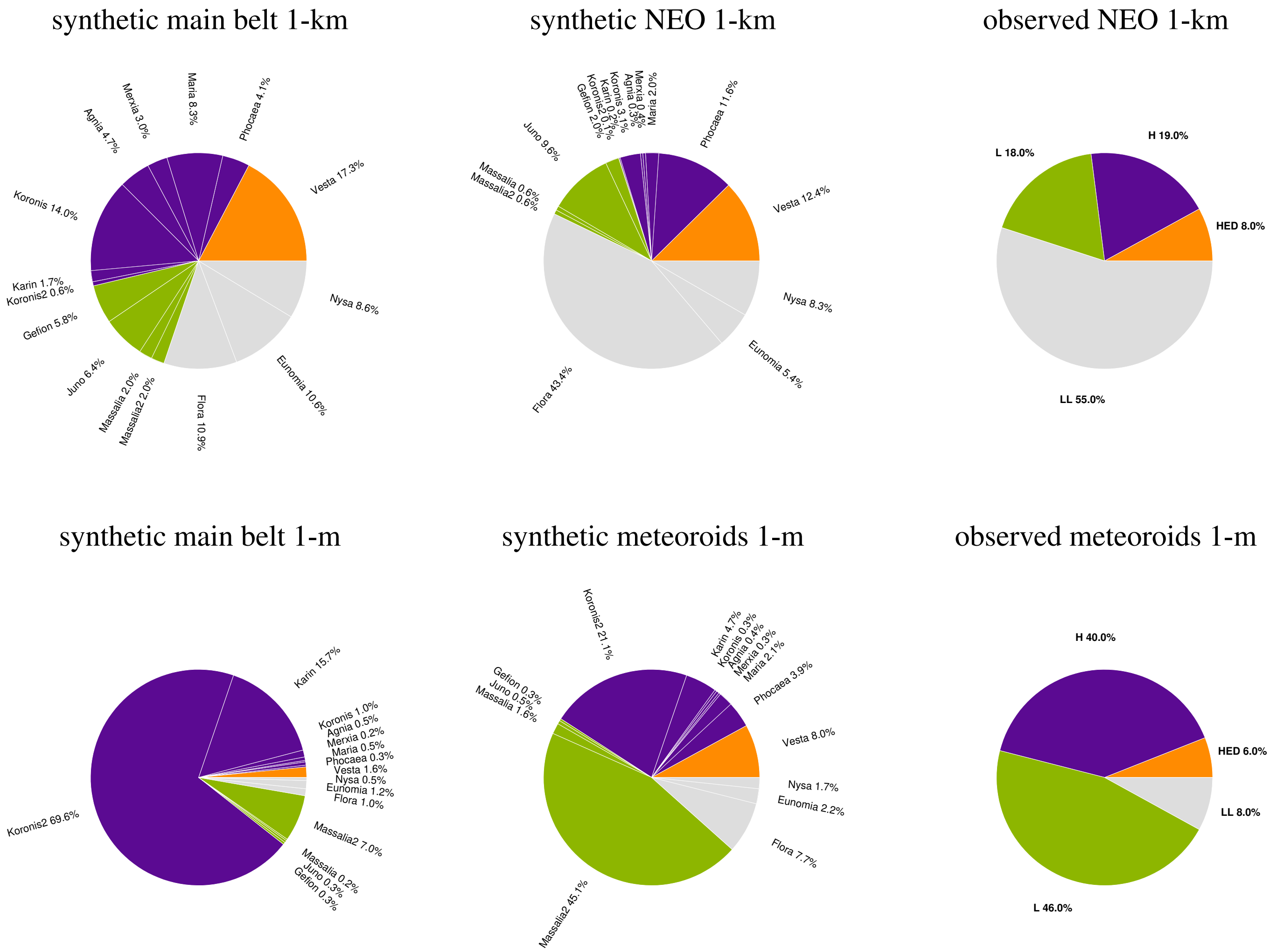

Figure 4: **Main sources of kilometre-sized S-type NEOs and ordinary chondrite meteorites.** Relative percentages of HED-, H-, L-, and LL-like bodies of the synthetic main belt (left), of the synthetic NEO (middle) and observed NEO (right) populations are compared. The contributions of individual families are indicated in the respective pie charts. For 1-km NEOs, our model indicates the total percentages of HED 12%, H 18%, L 12%, LL 58%. For 1-m meteroids, HED 8%, H 33%, L 47%, LL 12%. Our model is in agreement with the compositional distribution of NEOs [21] and the meteorite fall statistics [37].

Young asteroid families as the main source of meteorites (SI)

1 Family identification

We used recent catalogues (Jun 2021) to identify families. We combined the following datasets: Astorb [46], AFP [47,48], Wise [49], Akari [50], and SDSS [51], to obtain both orbital and physical data, whenever available. We applied the hierarchical clustering method (HCM; [52]) on proper orbital elements with a variable cut off velocity as the initial step, followed by an addition of halo (optional), and a removal of interlopers. Halo was used when a family merges with another family; this is mitigated by using bodies brighter than a suitable magnitude limit for the HCM and by adding fainter bodies, if their distance is smaller than another cut off velocity. Interlopers are recognised on the basis of physical data; unless specified otherwise, we assumed a geometric albedo $p_V \in (0.1; 0.5)$ and a Sloan colour index $a^\star \in (-0.1; 0.5)$. Additionally, we used the relation between the absolute magnitude H and the proper semimajor axis a_p [53]:

$$H(a_\mathrm{p}) = 5\log_{10}\frac{|a_\mathrm{p} - a_\mathrm{c}|}{C}\,, \tag{1}$$

where the parameter C determines the overall extent of the family. Bodies are removed if $H < H(a_\mathrm{p})$. The value of C is directly related to the upper limit of the age (but *not* to the age; [54]):

$$t_\uparrow = 1\,\mathrm{Gy}\,\frac{C}{10^{-4}\,\mathrm{au}}\left(\frac{a_\mathrm{c}}{2.5\,\mathrm{au}}\right)^2\frac{\rho}{2.5\,\mathrm{g\,cm^{-3}}}\left(\frac{0.2}{p_V}\right)^{1/2}. \tag{2}$$

Technical intermezzo. The Vesta family was associated at 100 m/s (core) and 100 m/s (halo). For the first step, we used only bodies with $H \le 15\,\mathrm{mag}$, for the second step $H > 15\,\mathrm{mag}$, so that the family is well separated from other families. Other parameters were: $a_\mathrm{c} = 2.36151\,\mathrm{au}$, $C = 3.0\times10^{-4}\,\mathrm{au}$, $p_V \in (0.1; 0.7)$, $a^\star \in (0; 0.5)$, $i - z \in (-0.85; -0.05)$. We considered (306) Unitas to be an interloper.

The Massalia family was associated at 30 m/s (core) and 100 m/s (halo); with $a_\mathrm{c} = 2.40863\,\mathrm{au}$, $C = 0.3\times10^{-4}\,\mathrm{au}$, $p_V \in (0.12; 0.6)$. It was a difficult case, because it is close to the Nysa/Polana complex and the 1:2 mean-motion resonance with Mars, which connects the two neighbouring families.

The Maria family was a simple case: $v = 55\,\mathrm{m/s}$, $a_\mathrm{c} = 2.55370\,\mathrm{au}$, $C = 2.3\times10^{-4}\,\mathrm{au}$.

The Merxia family too: $v = 50\,\mathrm{m/s}$; with $a_\mathrm{c} = 2.74513\,\mathrm{au}$, $C = 0.5 \times 10^{-4}\,\mathrm{au}$.

For the Agnia family, we had to choose a different central body (1020) Arcadia, located in the densest part, not (847) Agnia itself. The cut off velocities were 60 m/s (core), 80 m/s (halo); together with $a_\mathrm{c} = 2.79024\,\mathrm{au}$, $C = 0.17 \times 10^{-4}\,\mathrm{au}$. The family has a structure strongly affected by the z_1 secular resonance, along which the HCM associates bodies [55].

The Koronis family was associated at 55 m/s, and $a_\mathrm{c} = 2.86878\,\mathrm{au}$, $C = 4.3 \times 10^{-4}\,\mathrm{au}$. The family was extended beyond 2.96 au, i.e., the 7:3 mean-motion resonance with Jupiter, which fits well within the (a_p, H) envelope.

The Gefion family was a simple case: $v = 40\,\mathrm{m/s}$, $a_\mathrm{c} = 2.78381\,\mathrm{au}$, $C = 10^{-4}\,\mathrm{au}$.

The Juno family too: $v = 40\,\mathrm{m/s}$, $a_\mathrm{c} = 2.66938\,\mathrm{au}$, $C = 10^{-4}\,\mathrm{au}$.

For the Flora family, we used a <15-mag core at 110 m/s and a <20-mag halo at 100 m/s. Other parameters were $a_\mathrm{c} = 2.20145\,\mathrm{au}$, $C = 2.1 \times 10^{-4}\,\mathrm{au}$, $p_V \in (0.12; 0.6)$, $a^\star \in (0; 0.5)$, $i - z \in (-0.3; 0.5)$. It has a structure affected by the ν_6 secular resonance. Moreover, there is a persisting contamination from the Baptistina family.

The Eunomia family was associated at 40 m/s; with $a_\mathrm{c} = 2.64357\,\mathrm{au}$, $C = 2.3 \times 10^{-4}\,\mathrm{au}$. The (173) Ino family may be a part of Eunomia, just behind the 8:3 resonance. Possibly, this is also the case of (53546) 2000 BY_6.

The Nysa family is complicated, because of several overlapping families [56]. We used (135) Hertha as a central body, together with a 15-mag core at 80 m/s and a 20-mag halo at 100 m/s. We considered both (44) Nysa, (135) Hertha to be interlopers, given their reflectance spectra (E-, M-type). Moreover, we suppressed the contamination from the Polana family by $a_\mathrm{c} = 2.42851\,\mathrm{au}$, $C = 1.5 \times 10^{-4}\,\mathrm{au}$, $p_V \in (0.125; 0.5)$, and also $\sin I_\mathrm{p} \in (0; 0.053)$.

All families as they were identified are shown in Fig. 19. In order to compute diameters from magnitudes, we used either the measured albedos, or the median albedo of the respective families. The resulting SFDs are shown in Fig. 6.

Main belt population at 1 kilometre. We can directly compare the main-belt populations at 1 km, using a straightforward extrapolation from multi-kilometre sizes, because the new data allowed us to actually see the effect of observational bias. The latter affects the SFDs substantially at sub-km sizes for S-type populations, but at 1-km it can be 'safely' extrapolated from multi-kilometer sizes [57]. Approximate slopes derived for observed SFDs are listed in Tab. 1. For H-chondrite families (see Fig. 6, left), the sequence from most numerous to less numerous populations is (in units of 10^3 bodies):

Koronis (9.2) → Maria (5.5) → Agnia (3.1) → Phocaea (2.7) → Merxia (2.0) → Karin (1.1);

where we also included the Karin family (to be discussed in Sec. 6). For L-chondrite (middle):

Juno (4.2) → Gefion (3.8) → Massalia (2.6);

for LL-chondrite (right):

Flora (7.2) → Eunomia (7.0) → Nysa (5.7).

On the other hand, a simple extrapolation of SFDs down to 1 metre is not possible and we need a collisional model to do this properly.

2 Calibration of the collisional model

We used the collisional code called Boulder [28], which is a Monte-Carlo approach, working with binned differential mass distributions of an arbitrary number of populations. In our case, we used 3 populations: the main belt, one of the families and the NEO population. The Boulder code uses a number of parameters or relations describing how collisions between targets and projectiles produce fragments. The principal parameter is the critical impact specific energy $Q^\star(D)$ (in $\mathrm{J\,kg^{-1}}$), which is a function of the target size D. We used the formulation of [58] with modified parameters (as shown in Fig. 7):

$$Q^\star(D) = Q_0\,(D/2)^a + B\rho\,(D/2)^b\,, \tag{3}$$

where $Q_0 = 9\times 10^7$, $a = -0.53$, $B = 0.5$, $b = 1.36$ (all in cgs units when applicable). The density ρ was either $3\,\mathrm{g\,cm^{-3}}$, or specific (if known precisely; Appendix A). These parameters are within the range of values tested by [59]. Furthermore, relations for the largest remnant mass $M_{\mathrm{lr}}(Q)$, the largest fragment mass $M_{\mathrm{lf}}(Q)$, the slope of fragment size distribution $q(Q)$ are needed, where Q denotes the impact specific energy (also in $\mathrm{J\,kg^{-1}}$), as usually scaled by $Q^\star(D)$. For 100- and 10-km bodies, we used the relations described in [60,61], with a linear interpolation in between. The collisional probabilities and velocities for various combinations of populations are listed in Table 9. Because the evolution is stochastic, we always compute multiple (at least 10) runs to reject rare events (e.g., Ceres catastrophic disruptions).

Our collisional model is constrained by: (i) the observed main belt SFD [45], (ii) the NEO SFD [62], (iii) the Vesta family SFD, (iv) Rheasylvia basin's age 1 Gy [63], and (iv) (4) Vesta's cratering record [64], namely the heavily-cratered terrain (HCT) and the large diffuse craters (LDC). The final state of the model is shown in Fig. 9. As mentioned above, the $Q^\star(D)$ was adjusted in order to fit the *tail* of the observed main belt SFD. Otherwise, the synthetic populations 'undershoot' the observed ones (see Fig. 7).

We use a full transport matrix between all populations. In fact, transport is a complex process, driven by the Yarkovsky drift, the YORP effect, collisional reorientations, spin evolution, and gravitational resonances. In practice, the transport from the whole main belt → NEO space is characterized by a size-dependent mean decay time scale $\tau_{\rm mb}$. The time scale of main belt bodies must be relatively long, otherwise the NEO population is 'overshot' (see Fig. 8). On the other hand, the transport from the NEO → trash bin is on average very short ($8\,{\rm My}$), which is comparable to [17] (6 to 11 My; see their Fig. 15).

The nominal time span of our simulations is 4.4 Gy, to leave some space for the early evolution, without solving a question: whether the evolution was very early or not (cf. [65]). Of course, cratering may also be produced very early, but hereinafter we assume no saturation and no crater erasure for simplicity. Consequently, we should never 'overshoot' the observed record.

Our modelling certainly has some caveats. For example, it is not certain whether the initial SFD of the early main belt should be broken at 20 km, or at 15 km; the initial slope q in the size range $D \in (10; 100)\,{\rm km}$ could possibly be steeper; the average density could be $2\,{\rm g\,cm^{-3}}$ instead of $3\,{\rm g\,cm^{-3}}$; possibly, there are two or even more rheologies for S- and C-type populations; the YORP spin-up may destroy bodies instead of affecting transport; etc.

3 Extrapolated size distributions

For each of the families, the collisional model must be set up individually. The initial conditions correspond to the age of the family, which is unknown. Consequently, both the main belt and the family SFDs must be adapted, so that the final conditions correspond to the observations. The SFD was characterized by the largest remnant (LR), the largest fragment (LF), and the power-law cumulative slopes: q_a, q_b, q_c, q_d, with the diameter ranges specified by: D_1, D_2, D_3. Again, every model was run at least 10 times to determine its uncertainties, which are mostly due to the stochasticity of collisions, or break-ups of large asteroids with a fractional probability. We always tried to use the simplest initial conditions possible, i.e., a simple power law $q_\mathrm{a} = q_\mathrm{b}$, which subsequently 'breaks' in the course of collisional evolution, $q_\mathrm{a} > q_\mathrm{b}$, because it reaches equilibrium with the background population. The values of q_c or q_d should be less steep than -3 to prevent a divergence of mass (cf. Sec. 6). If it did not work, because the initial conditions were not simple, we prepared a more complicated model(s). Generally speaking, the use of collisional evolution to constrain the age of asteroid families dates back to the work of [66]. Here, we profit from having information about SFDs down to significantly smaller sizes than three decades ago.

Our results for relatively young families (Merxia, Agnia, Juno), as well as some old families (Vesta, Koronis, Flora) suggest the possibility that their SFDs were initially simple power-laws, starting at the largest fragment and ending even below the observational incompleteness threshold (see Fig. 10). Ages of these families are easy to estimate (see Table 2). We wait until the SFD 'breaks' to two power-laws and fits the observed SFD. The break is induced by main belt ↔ family or secondary collisions and typically occurs at $D \doteq 5\,\mathrm{km}$.

However, the remaining families (Massalia, Maria, Gefion, Eunomia) required more complicated initial conditions, as demonstrated in Fig. 10. It may also indicate a different age, or a mismatch between collisional and orbital models. The ages derived from orbital models are discussed in Appendix B.

Technical intermezzo. Maria's synthetic SFD often 'undershoots' the observed one at $D \simeq 1\,\mathrm{km}$ which would correspond to an age younger than 2500 My (not to 3000 My as suggested by orbital models); it is also very shallow at large sizes, which is typical for populations of objects including interlopers.

Gefion's SFD often 'overshoots' for its previously proposed age of 470 My [67] and the only way to fit observations is again using a broken power-law. On the other hand, if the initial SFD is a simple power-law $q_\mathrm{a} = q_\mathrm{b} = -4.6$, the best-fit is obtained naturally for 1500 My which might be more compatible with [68].

In the case of Massalia, a broken power-law must be used to obtain a fit at 150 My [53]. For a simple power-law with the cumulative slopes $q_\mathrm{a} = q_\mathrm{b} = -7.5$, the age would be as long as 800 My.

Eunomia's SFD at $D \simeq 20\,\mathrm{km}$ is wavy, which is either related to the primordial SFD, or the presence of interlopers. Its SFD at multi-km sizes is very shallow, actually the most shallow of all families, which indicates a significant depletion of objects and a preference for an older age (definitely more than 3000 My).

Taken overall, ages seem to be self-consistent; none is older than 4.4 Gy and they are distributed over the whole interval from 0 to 4.4 Gy.

Main belt population at 1 metre. For metre-sized bodies, there is inevitably some stochasticity, leading to about half-order variation from simulation to simulation in the absolute number of bodies, due to secondary collisions and temporally variable tail. Consequently, for H-chondrite families, the populations are (in 10^{10} units):

Karin (30-60) $\rightarrow$ Koronis (2-4) $\rightarrow$ Maria (0.8-2) $\rightarrow$ Agnia (1-2) $\rightarrow$ Phocaea (0.5-1) $\rightarrow$ Merxia (0.3-0.9);

for L-chondrite:

Juno (0.5-1.5) $\rightarrow$ Gefion (0.5-1.5) $\rightarrow$ Massalia (0.4-1);

for LL-chondrite:

Eunomia (1-6) $\rightarrow$ Flora (2-4) $\rightarrow$ Nysa (1-1.6).

For Karin, see again Sec. 6 . Otherwise, the order is similar for metre- and kilometre-sized bodies. Maria is similar to Agnia within stochasticity; Juno to Gefion or Massalia; Eunomia might be slightly more populous than Flora. None of these results is dependent on the precise family age, because we always fit the currently observed SFD. Let us recall that, at this stage, all the populations are still in the main belt; a transport is yet to be applied.

4 NEO population at 1 kilometre

We used our orbital model described in [31] to determine the decay time scales in the main belt and the life times among the NEOs. It is based on the symplectic integrator SWIFT-RMVS3 [32].

Table 1: Power-law slopes of the observed SFDs of the S-type families.

family	q_1	q_2	q_3
Vesta (HED)	-4.6	-3.3	-1.5
Phocaea (H)	-2.7	-1.4	
Maria (H)	-2.0	-2.7	-1.5
Merxia (H)	-3.2	-2.5	
Agnia (H)	-3.2	-3.0	-2.7
Koronis (H)	-2.5	-1.5	
Karin (H)	-4.2	-2.9	
Massalia (L)	-5.7	-3.4	-2.8
Gefion (L)	-3.9	-1.7	-1.2
Juno (L)	-2.8	-3.7	-3.1
Flora (LL)	-3.8	-2.8	-1.3
Eunomia (LL)	-4.5	-3.2	-1.2
Nysa (LL)	-8.9	-4.3	-1.7

Table 2: Ages of the S-type families estimated from our collisional model.

family –	age My
Vesta (HED)	1100 ± 100
Phocaea (H)	700 ± 100
Maria (H)	2500 ± 300
Merxia (H)	330 ± 50
Agnia (H)	100 ± 50
Koronis (H)	2200 ± 300
Massalia (L)	800 ± 100
Gefion (L)	1500 ± 200
Juno (L)	750 ± 100
Flora (LL)	1200 ± 200
Eunomia (LL)	4200 ± 300
Nysa (LL)	600 ± 100

The dynamical model includes: 11 mutually interacting bodies (Sun, Mercury to Neptune, Ceres, Vesta), the Yarkovsky effect [34,35], the YORP effect [36], collisional reorientations, a mass shedding, and the strength-dependent spin limit [69]. This is supplemented by a series of digital filters to compute mean elements [70] and proper elements [71].

Some of the parameter values were common for all simulations. Namely, a time step $\Delta t = 9.13125\,\mathrm{d}$, output of osculating elements $10\,\mathrm{ky}$, sampling of osculating elements $1\,\mathrm{y}$, sequence of filters A, A, A, B, decimation factors 10, 10, 10, 3, output of mean elements $3000\,\mathrm{y}$, number of samples for the Fourier transform 1024, output of proper elements $0.1\,\mathrm{My}$, a thermal capacity $C = 680\,\mathrm{J\,kg^{-1}\,K^{-1}}$, thermal conductivity $K = 10^{-3}\,\mathrm{W\,m^{-1}\,K^{-1}}$, thermal emissivity $\epsilon = 0.9$, Bond albedo $A = 0.1$, surface density $\rho = 1.5\,\mathrm{g\,cm^{-3}}$, YORP efficiency $c_{\mathrm{YORP}} = 0.33$, reorientation time scale $B = 84.5\,\mathrm{ky}$, with exponents $\beta_1 = 0.83$, $\beta_2 = 1.33$, and normalisations $\omega_0 = 3.49 \times 10^{-4}\,\mathrm{rad\,s^{-1}}$, $D_0 = 2.0\,\mathrm{m}$, cohesive strength scale $\kappa = 2.27 \times 10^7\,\mathrm{g\,cm^{-1/2}\,s^{-2}}$, friction coefficient $s = 0.25$, relative axial ratios $c/a = 0.7$, $b/a = 0.7$, ...

Others were specific, adapted for individual families. We always tried to create an initial synthetic family in such a way that – after the long-term evolution – it ends up as similar to the observed family (see, e.g., [72]). Parameters of the principal bodies ('parent bodies') are discussed in Appendix A. Probably the most important choice is the initial velocity field. According to the rule: 'either escape or not escape', we created a distribution with the peak at about the escape speed v_{esc} from the respective parent body. For simplicity, we assumed an isotropic field (even a cratering is approximately isotropic in shifted coordinates). Moreover, we assumed a size-dependent relation [53]:

$$v(D) = v_5 \left(\frac{D}{D_5}\right)^{\alpha} . \tag{4}$$

The geometry in the $(a, e, \sin I)$ space is further determined by the true anomaly f and the argument of pericentre ω. Sometimes, these are still visible in the observed distribution of elements. This is true not only for Karin, but also for much older families [72,73]. These parameters are listed in Tab. 3

The results of our simulations are summarized in Fig. 11, Fig. 12, and the respective time scales are listed in Table 4.

Table 3: Parameters of the synthetic families used in our orbital models.

family	v_5	D_5	α	f	ω
–	$\mathrm{m\,s^{-1}}$	km		deg	deg
Vesta (HED)	200	2	-0.5	90	120
Phocaea (H)	30	5	-0.5	30	0
Maria (H)	50	5	-0.5	90	90
Merxia (H)	24	5	-0.5	90	90
Agnia (H)	15	5	-0.5	30	0
Koronis (H)	50	5	-0.5	30	30
Karin (H)	5	5	-0.5	30	0
Massalia (L)	24	5	-1.0	90	130
Gefion (L)	100	2	-0.5	90	30
Juno (L)	100	2	-0.5	90	30
Flora (LL)	100	2	-0.5	90	90
Eunomia (LL)	100?	2?	0.0	90	50
Nysa (LL)	35	5	-0.5	135	0

Notes. v_5 denotes the ejection velocity, D_5 the reference size, α the exponent of the distribution, f the true anomaly, ω the argument of pericentre.

Steady-state situation. To estimate the number of 1-km bodies in the NEO population, we can assume a steady state. In this situation:

$$N_{\rm neo}(>1\,{\rm km}\,|\,{\rm H}) = \int_0^\infty C N_{\rm mb}(>1\,{\rm km})\,p({\rm H})\,\frac{f(\tau_{\rm neo})\tau_{\rm neo}{\rm d}\tau_{\rm neo}}{\tau_{\rm mb}}\,, \tag{5}$$

where C denotes the calibration, p the probability that the family contributes to an H-like population, $\tau_{\rm neo}$ the life time in the NEO population, f the corresponding distribution function, and $\tau_{\rm mb}$ the life time in the main belt population; and similarly for 1-m size and similarly for L-like, LL-like. For constant factors, Eq. (5) simplifies to:

$$N_{\rm neo}(>1\,{\rm km}\,|\,{\rm H}) = C N_{\rm mb}(>1\,{\rm km})\,p({\rm H})\,\frac{\bar{\tau}_{\rm neo}}{\tau_{\rm mb}}\,, \tag{6}$$

where $\bar{\tau}_{\rm neo}$ denotes the mean lifetime in the NEO population. Actually, this is the very reason why the median must *not* be used. However, short-lived NEO orbits are common and long-lived ones are exceptional (see Fig. 12). In other words — outliers determine the mean value. One solution is to use a as many orbits as possible (or orbital clones). However, the total number of bodies entering the NEO region is limited, because we study individual families. In other words — a poor sampling of τ's (hence low $\bar{\tau}$) may be more realistic than fine sampling (high $\bar{\tau}$).

Moreover, the NEO orbits sometimes require a very fine time step (0.25 d), if the eccentricity is extreme [17]; this problem is especially urgent for the ν_6 resonance, which pushes $e \to 1$. For some families (Flora) we thus used $\tau_{\rm g18}$ from Tab. 4. Alternatively, the values of τ's differ from [17], because some families (Flora) were identified as dense clusters, but they might be more extended, with bodies scattered across the ν_6 resonances.

Today, the Flora family seems to provide a dominant contribution to the population of kilometre-sized NEOs, followed by Vesta, Phocaea, Juno. This approximately corresponds to the percentages of observed NEOs. However, we should take into account also the background population which might be substantial. It is probably not surprising, because the 11 families discussed in this work only contain 54.1×10^3 of S-type 1-km bodies out of $\sim 231\times10^3$ present in the main belt, i.e., less than one fourth. One possible interpretation is that the background population is indeed spectrally similar to the families (cf. the "crime scene" figure in [54]).

Non-stationary situation. If we relax the assumption above, we have to compute the dynamical decay and transport from the main belt $\to$ NEO as non-stationary:

$$\dot{N}_i = -\frac{1}{\tau_i} N_i\,, \tag{7}$$

$$\dot{N}_j = +\frac{1}{\tau_i} N_i - \frac{1}{\tau_j} N_j \,, \tag{8}$$

where the index $i = 1..M$ corresponds to the families, $j = 1..M$ to the NEO populations, respectively. If $\dot{N}_j = 0$ is assumed, Eq. (8) simplifies to Eq. (6).

To demonstrate how contributions change in the course of time, due to dynamical decay alone, we solved the set of Eqs. (7) and (8), and plotted the solution in Fig. 15. Of course, a collisional decay occurs at the same time; it should be solved self-consistently by a collisional model. Nevertheless, Fig. 15 suggests that family contributions to the NEO population in the past must have been variable. It may also suggest a lower collisional activity between approximately 4 and 2.5 Gy ago, but it sensitively depends on the individual ages of the families (cf. Sec. 8).

Given the overall decay of individual families (both collisional and orbital), they can hardly be always in an steady state. If true, Eq. (6) is questionable, as so is the very method for estimation of the NEO population, because we do not know the derivatives $\dot{N}_j$'s. In principle, we can use the observations to determine N_j's and compute $\dot{N}_j$'s, but not the other way around.

5 NEO population at 1 metre

The evolution of metre-sized bodies was computed in the same way. Their initial conditions were modified though — we used the current orbits of family members, because these fragments are continuously replenished by collisions. The time span is relatively short, $50\,\mathrm{My}$, which is sufficient to measure the decay time scale. Our results are summarised in Fig. 13, Fig. 14, and in Tab. 5.

The situation is more complex for metre-sized bodies compared to the km-size ones. There are inevitable uncertainties stemming from a variable 'tail' of the SFDs. HED and LL-chondrite-like families contribute comparably: Vesta 4.3-15.2 $\times$ 10^8, Flora 6.3-12.5 $\times$ 10^8, in agreement with the observations. If the absolute number of *all* metre-sized NEOs is 200-300 $\times 10^8$ [74], and the percentages of meteorite classes HED 6.2 %, LL 8.2 %, one would expect 12.4-18.6 $\times 10^8$, 16.4-24.6 $\times 10^8$, respectively. This is not far from our synthetic numbers, given the fact that scattered V-types (not associated with Vesta) also contribute to HED and that other families (Eunomia, Nysa) also contribute to LL. For simplicity, we assumed that the percentages of meteorites correspond to the percentages of meteoroids. Nevertheless, we also computed the flux (in $10^{-9}\,\mathrm{y}^{-1}\,\mathrm{km}^{-2}$ units):

$$\Phi = p N_{\mathrm{neo}}(>1\,\mathrm{m}) \,, \tag{9}$$

where p is the collisional probability of meteoroids with the Earth, evaluated from our orbital simulations of metre-sized bodies (Tab. 10). It turns out that at least for the most relevant families the fluxes are not so different from populations (see Tab. 11); with the obvious exception of Phocaea. Moreover, some meteoroids might be more fragile (e.g., carbonaceous chondrites), and preferentially disintegrate during their atmospheric entry, which would decrease the absolute numbers above.

On the contrary, H- and L-chondrite-like bodies are underestimated compared to the observations. If the percentages are H 33.8 %, L 37.0 %, one would expect up to 67-101 $\times 10^8$, 74-111 $\times 10^8$ bodies, respectively. This is different by a factor of more than ~ 10. While this is a serious mismatch ('conundrum'), it is a confirmation that the background or other families, possibly much younger, should be taken more seriously.

6 The Karin collisional series

As an example of a possible contribution of young families, we studied the Karin family = FIN 610 [54], i.e., a secondary breakup in the Koronis family (H) with an age of 5.8 My [76,77]. It contains 1.1×10^3 kilometre-sized bodies and up to 30 to 60×10^{10} metre-sized bodies. It is clearly a non-steady population.

Contrary to our expectations, the Karin family may contribute more than any other family to the population of metre-sized bodies if its initial SFD was a power-law with the cumulative slope -2.9 down to 1 m. Indeed, the observed SFD is a *perfect* power-law down to the observational completeness (Fig. 16) and the 'tail' of the SFD simply had not enough time to evolve; it takes 30 My to decrease below Koronis (Fig. 3).

An important question is: is there enough time to deliver bodies to the NEO space? Yes and no. The expected Yarkovsky drift rate (without YORP) is up to 0.0003 and $0.06\,\mathrm{au\,My^{-1}}$, for 1-km and 1-m bodies, respectively. The distance to the neighbouring resonance 5:2 is 0.03 to $0.05\,\mathrm{au}$. Consequently, it would take about 100 My, until kilometre-sized bodies are delivered, but only a few My for metre-sized bodies, depending on their spin axis orientations.

Alternatively, one can assume that metre-sized fragments were ejected at significantly larger speeds, as in Eq. (4). This would make an even early transport possible. It is closely related to an equipartition of kinetic energy between high-mass and low-mass fragments, as seen in some SPH simulations of break-ups [78]. Nevertheless, most fragments colliding with the Earth today must have been travelling in space for approximately 5.8 My.

Table 4: Dynamical time scales and cumulative numbers of 1-km asteroids in the main belt (mb) and the near-Earth region (neo).

family	res.	τ_{g18}	1-km τ_{neo}	1-km τ_{mb}	ρ	1-km N_{mb}	1-km N_{neo}	obs.	obs.
–	–	My	My	My	$g\,cm^{-3}$	10^3	1	1	%
Vesta (HED)	ν_6	6.98	3.22	1711	2.5!	11.4	21.4	24	8
Phocaea (H)	ν_6	6.98	5.91	796	2.5	2.7	20.0!	6	2
Maria (H)	3:1	1.83	0.95^4	1524	3.0	5.5	3.4	17	5
Merxia (H)	5:2	0.68	0.22	596	2.5	2.0	0.7	12	4
Agnia (H)	5:2	0.68	0.19	1004	2.5	3.1	0.6	12	4
Koronis (H)	5:2	0.68	0.81^4	1404	3.0	9.2	5.3	12	4
Karin (H)	5:2	0.68	0.22^u	921^a	2.5	1.1	0.3	–	–
Massalia (L)	3:1	1.83	0.45	1018	2.5!	2.6	1.1	16	5
Gefion (L)	5:2	0.68	0.69	760	2.5!	3.8	3.5	11	4
Juno (L)	8:3	1.70	2.49	627	2.5	4.2	16.6	29	9
Flora (LL)	ν_6	6.98	0.37^6	669	2.5	7.2	**75.1**	**158**	51
Eunomia (LL)	3:1	1.83	4.48	3335	3.54	7.0	9.4	14	5
Nysa (LL)	3:1	1.83	2.34	720	2.5	5.7	18.5	–	–
HED							21.4	24	8
H							31.7	59	19
L							21.3	56	18
LL							103	172	55
H+L+LL						54.1!	156!	287?	91
all S-types						231?		287?	
all bodies						1360		925	

Notes. For all families, we report the neighbouring resonances, the NEO life time τ_{g18} from [17], the NEO life times τ_{neo} from this work, computed for 1-km bodies, the main belt life times τ_{mb}, the volumetric density of simulated bodies, the observed cumulative number $N_{mb}(>1\,km)$ of main belt bodies, the computed cumulative number N_{neo} of NEOs and meteoroids, along with the observed N_{neo} from [39], where the original percentages were multiplied by the total number of S-type NEOs ($925 \times 31\,\% \doteq 287$; [21]). For comparison, the fraction of S-type main belt bodies is different ($1360 \times 10^3 \times 17\,\% \doteq 231 \times 10^3$; [75]). Additional notes: ^{4} 4 outer planets; ^{u} undersampled; ^{a} after 100 My; ^{6} problem with the ν_6 resonance (τ_{g18} is used instead of τ_{neo}).

Table 5: Same as Tab. 4 for 1-m meteoroids.

family	res.	τ_{g18}	1-m τ_{neo}	1-m τ_{mb}	ρ	1-m N_{mb}	1-m N_{neo}	obs.	obs.
–	–	My	My	My	$g\,cm^{-3}$	10^{10}	10^{8}	10^{8}	%
Vesta (HED)	ν_6	6.98	2.50	115	2.5!	2-7	4.3-15.2		6
Phocaea (H)	ν_6	6.98	7.24	114	2.5	0.5-1	3.2-6.4!		2
Maria (H)	3:1	1.83	1.82	98	2.5	0.8-2	1.5-3.7		15
Merxia (H)	5:2	0.68	0.43	81	2.5	0.3-0.9	0.2-0.5		7
Agnia (H)	5:2	0.68	0.34	103	2.5	1-2	0.3-0.7		8
Koronis (H)	5:2	0.68	0.26	201	2.5	2-4	0.3-0.5		8
Karin (H)	5:2	0.68	0.27	149	2.5	30-60	3.9-7.8!		–
Massalia (L)	3:1	1.83	3.83	139	2.5!	0.4-1	1.1-2.8		17
Gefion (L)	5:2	0.68	0.32	75	2.5!	0.5-1.5	0.2-0.6		6
Juno (L)	8:3	1.70	1.38	204	2.5	0.5-1.5	0.3-1.0!		**23**
Flora (LL)	ν_6	6.98	3.45	110	2.5	2-4	**6.3-12.5**		7
Eunomia (LL)	3:1	1.83	1.56	199	2.5!	1-6	0.8-4.7		1
Nysa (LL)	3:1	1.83	1.79	114	2.5!	1-1.6	1.6-2.5		
HED							4.3-15.2	10-15	6
H							9.4-19.6!	67-100	40
L							1.6-4.4!	77-116	46
LL							8.7-19.7	13-20	8
H+L+LL						40.0-85.5	19.7-43.7	158-237?	94
all S-types								158-237?	
all bodies						400-1200	400-800	**200-300**^{H}	
with 2nd Koronis:									
Koronis$_{(2)}$	5:2	0.68	0.26	201	2.5	∼100-300?	12.9-38.8		–
H							22.3-58.4	67-100	40
with 2nd Massalia:									
Massalia$_{(2)}$	3:1	1.83	3.83	139	2.5!	∼10-30?	27.6-82.7		–
L							29.2-87.1	77-116	46

Notes. The observed *percentages* of meteorites from [39] For comparison, the observed percentages of meteorite falls from `https://www.lpi.usra.edu/meteor/`, `https://metbase.org/` with respect to *all* classes are: HED 6.2 %, H 33.8 %, L 37.0 %, LL 8.2 %, respectively. Additional notes: ^{H} [74].

Moreover, according to our analysis of Karin, there is not a single sub-family, but four. The second one is $\text{Koronis}_{(2)}$ = FIN 621 [26], originating from a cratering event on Koronis itself. Its SFD is even steeper (-4.0; Fig. 16), so that it likely dominates Karin already at $D \lesssim 0.5\,\text{km}$. In addition, we discovered a third and a fourth family when looking at the $a_\text{p}, e_\text{p}, \sin I_\text{p}$ distribution from a suitable direction. The concentration or correlation of orbits is shown in Fig. 1. They are logically more dispersed, as small fragments have already reached the resonances (5:2, 17:7). It is a confirmation that such collisions are still ongoing within the parent family (i.e., $\text{Koronis}_{(1)}$).

In other families, like Eunomia, these sub-clusters are not seen, which is an argument in favour of the collisional cascade being driven by secondary collisions. However, we should estimate it explicitly (in the same way as in our collisional model). A projectile of diameter d is needed to disrupt a target of diameter D:

$$d = D \left(\frac{2Q}{v^2} \right)^{\frac{1}{3}} , \tag{10}$$

where Q is the specific energy and v the projectile speed. The frequency of collisions (in y^{-1}) is:

$$f = p \frac{D^2}{4} f_\text{g} N(>D)\, N(>d)\,, \tag{11}$$

where p denotes the intrinsic collisional probability (in $\text{km}^{-2}\,\text{y}^{-1}$; Tab. 9), f_g the gravitational focussing factor, and N's the respective numbers of available targets and projectiles. For main belt–main belt collisions, $D = 30\,\text{km}$, $Q = Q^\star$ (i.e., catastrophic disruptions), $d = 3.9\,\text{km}$, $N(>D) = 1330$, $N(>d) = 129000$, we obtain $f = 1.1 \times 10^{-7}\,\text{y}^{-1}$, or $1/f = 9\,\text{My}$. Consequently, it is not surprising that we observe a Karin-like event.

On the other hand, Koronis–Koronis collisions occur with much higher probabilities (Tab. 9), lower impact speeds, and much lower numbers of bodies; $d = 9.1\,\text{km}$, $N(>D) = 10$, $N(>d) = 145$, hence $f = 4.3 \times 10^{-12}\,\text{y}^{-1}$. What we see in Koronis is not a cascade of secondary collisions, but rather a series of primary collisions.

There might still be some caveats in our estimates: (i) the Karin and $\text{Koronis}_{(2)}$ families had similar nodes and similar precession rates, while p's were computed for a uniform distribution of nodes; (ii) even cratering events ($Q \ll Q^\star$) are capable of producing numerous fragments; (iii) a population of sub-km asteroids may have a different spatial distribution as well as p's with respect to Koronis; (iv) a production of S-type metre-sized fragments might have been temporarily increased by another collisions (e.g., with CM-type fragments from the Veritas family; [40]).

Nevertheless, if Karin-like events remain observable for at least $50\,\text{My}$, we predict there should be more than 5 of them in the whole belt. Moreover, if such events produce steep SFD's, as suggested by Fig. 16, they certainly dominate Koronis-like families at sub-km sizes as well as at metre sizes via a collisional cascade.

7 7.5 My age for Koronis$_{(2)}$

In order to estimate the age of the Koronis$_{(2)}$ family, we used a backward integration and a convergence of orbits, namely of the angles Ω, or ω. Our dynamical model was similar and simplified, by assuming only 5 massive bodies (Sun and the four giant planets). We applied a barycentric correction and a rotation to the Laplace plane. We used 100 orbits, corresponding to the Koronis$_{(2)}$ family members, with 20 clones for each of them, sampling a uniform distribution of the obliquity $(\cos\gamma)$.

The Yarkovsky effect was included, with the thermal parameters suitable for S-type bodies covered by regolith: the bulk density $\rho = 2.5\,\mathrm{g\,cm^{-3}}$, the surface density $\rho_\mathrm{s} = 1.5\,\mathrm{g\,cm^{-3}}$, the thermal conductivity $K = 10^{-3}\,\mathrm{W\,m^{-1}\,K^{-1}}$, the heat capacity $C = 680\,\mathrm{J\,kg^{-1}\,K^{-1}}$, Bond albedo $A = 0.1$, and the thermal emissivity $\epsilon = 0.9$. Drift rates reach up to $\dot{a} = 0.0015\,\mathrm{au\,My^{-1}}$. The YORP effect is not important on this time scale (cf. [77]). A collisional reorientation is again not important.

We used the symplectic integrator MVS2 from the SWIFT package [32]. The time step was 18.2625 d. We computed the mean elements [70] by sampling of the osculating ones every 1 y, with a sequence of filters A, A, B and decimation factors 10, 10, 3. The output step was thus 300 y, in order to suppress oscillation on the orbital time scale but not secular. The total time span was 20 My.

Importantly, we improved a post-processing: (i) for each time step, we computed the differences of angles $\Delta\Omega$ (or $\Delta\omega$) with respect to a reference body (e.g., (158) Koronis); (ii) we chose the best clone for each body; (iii) we sorted selected clones according to $|\Delta\Omega|$; (iv) we chose the percentage of bodies, which will be discarded as interlopers, because it is inevitable that a family contains a percentage of interlopers (e.g., from Karin). (v) The result is 'a subset of a set of selected clones', for which we compute the median and range, because 'outliers' actually determine the age, not 'ordinaries', which remain close to the reference body.

A verification was done by the Karin family [7]. As possible checks, one can assert that the median is close to 0, the spins of clones are evenly distributed, other angles $(\Delta\omega)$ also converge, or that interlopers do not converge (or converge elsewhere).

The Koronis$_{(2)}$ family exhibits a clear convergence for the age $(7.5 \pm 0.1)\,\mathrm{My}$ (see Fig. 2). If the interloper percentage is 50%, which represents 50 converging orbits, the range is only 7°. Because a random range is approximately 180° (i.e., $\pm 90^\circ$), it is definitely not random, but a very systematic convergence. The resulting age would be the same for 20% (80 orbits), but the range (up to 100°) is not realistic. It is impossible to use only 10 orbits, because some of them do not converge. It is impossible to not remove interlopers, because there are interlopers. A systematic uncertainty of the order of 0.5 My is determined by the Yarkovsky effect, in particular the uncertainty of bulk density σ_ρ; to a lesser extent, by other thermal parameters.

Finally, we list 50 converging asteroids (out of 100):

158, 79975, 84465, 87289, 91688, 93840, 117887, 121652, 136781, 140302, 143047, 144159, 144614, 146657, 150050, 159121, 159210, 161809, 163638, 170802, 171639, 179248, 180965, 181144, 182760, 185001, 188109, 188754, 190445, 192102, 196852, 199593, 199681, 202266, 202537, 202603, 202763, 202809, 206118, 209361, 211804, 214679, 214835, 218049, 221394, 223407, 225057, 226815, 227509, 229655.

8 Discussion

IRAS dust bands. The Karin family event produced also dust, which was observed by IRAS as the 2.1° band of infrared radiation [8,9,27], i.e., at exactly the same inclination as the family. The equivalent diameter of all dust particles is approximately $D \simeq 11\,\mathrm{km}$ ([27], cf. Tab. 6). According to the Long Duration Exposure Facility (LDEF; [79]), the dominant size of dust particles is $d = 100\,\mu\mathrm{m}$, which corresponds to a number of particles $N(>100\,\mu\mathrm{m}) = 1.3 \times 10^{24}$.

Our extrapolated SFD of the Karin family, with the slope -2.9 determined for multi-kilometre asteroids, predicts the number of particles $N(>100\,\mu\mathrm{m}) = 2.7 \times 10^{23}$, which is surprisingly close to the IRAS value (see Fig. 3). In other words, our SFD seems to be reliable over 8 orders of magnitude.

The factor of ~ 5 difference indicates that the SFD slope is (was) even steeper, possibly close to -3.0. This is a special value, because it corresponds to a log-uniform distribution in mass. In math, it results from a reciprocal of a uniform random variable, $\frac{1}{x}$. In our case, every order of magnitude in size (10 km–1 km, 1 km–100 m, … 1 mm–100 μm) contains about the same amount of mass. The equivalent diameter of all orders is only $8^{1/3} = 2$ times larger. It is *not* divergent in mass, simply because we do not continue to 0.

For Koronis$_{(2)}$, a straight extrapolation to $100\,\mu\mathrm{m}$ is impossible, because its slope is too steep (-4.0); it cannot be kept due to very frequent collisions. If one extrapolates the SFD just by one order of magnitude to 0.1 km, and assume a collisional equilibrium with the main belt (-2.7), it turns out that Koronis$_{(2)}$ also contributes to the 2.1° dust band, but it can be hardly distinguished from Karin.

Interestingly, the inclination of (20) Massalia corresponds exactly to one of the dust bands, namely at 1.4° ([27], Fig. 19). This association is much more likely than with (656) Beagle [80], because the temperature profile, constrained by IRAS 12-, 24- and 60-$\mu\mathrm{m}$ band observations, indicates hotter dust grains. If true, the Massalia family (or its part) is younger than previously thought. As discussed in [39], the Massalia family slope -2.8 seems to be in agreement with the dust population, $N(>100\,\mu\mathrm{m}) \simeq 4 \times 10^{23}$ (see also their fig. 4).

Radiometric shock ages. Measured shock ages of OCs reveal non-uniform distributions, including some 'peaks' [81]. In some cases, these peaks might relate to very precise measurements, but at least some of them are real peaks. Do they correspond 1:1 to family-formation events? A 'nihilistic' answer would be no; or not necessarily. Nevertheless, for the moment, let us assume yes.

A possible correspondence is summarized in Tab. 7. All mineralogical groups of OCs include numerous shock ages around 4560 My, most likely related to accretion. For H-chondrite families, there are logical candidates for relatively young shock ages. Old shock ages might be related to Maria, Koronis, if these families are about 50 % older. This is indeed possible if the initial SFDs were about 50 % more populous.

For L-chondrite shock age 470 My, there is a known candidate the Gefion family [67], but its SFD indicates much older age (cf. Tab. B). A viable alternative might be the Juno family. Note: (3) Juno is the 2nd largest S-type asteroid. As discussed in [39], however, an even better alternative is the the Massalia family, suitably located in the inner main belt.

For LL-chondrite, there are two minor peaks, possibly related to Nysa or Flora. On the other hand, the major peak at 4200 My might be related to Eunomia. Note: (15) Eunomia is the 1st largest S-type asteroid.

Unfortunately, the sample of [81] is still limited. Ideally, one should have multiple meteorites with the same shock age, or more importantly, statistically significant 'gaps' in between, similar to the one between 1500 and 3500 My for H chondrites. Moreover, one cannot exclude the possibility that shocks originated in secondary collisional cascade, minor cratering events, microimpacts, etc.

Radiometric cosmic-ray exposure ages. Similarly, OCs have measured cosmic-ray exposure ages [12], which are unevenly distributed. A correspondence with recent family-formation events is summarized in Tab. 8. For the prominent H-chondrite peak between 6-8 My, by far the best candidates are the Karin and $\text{Koronis}_{(2)}$ families, as indicated by a convergence of orbits (Sect. 7). For the remaining distribution, the most likely source is the rest of Karin series.

Unfortunately, the L-, LL-chondrites peaks are much less prominent and the distributions seem to be broad. The range from 10 to 40 My is characteristic for collisional or transport time scales of metre-sized bodies. According to the dust bands (Sect. 8), the only possibility seems to be the young Massalia family, which age should coincide with the upper limit.

Table 6: Possible correspondence of dust bands and family-formation events.

band	D	family
–	km	–
1.4°	4	Massalia$_{(2)}$ (L)
2.1°	11	Karin series (H)
9.8°	14	Veritas (C)
all	$\sim$21	asteroidal dust
all	46	zodiacal cloud

Notes. D denotes the equivalent diameter of all dust particles from [27]; where 'asteroidal' means without Jupiter-family comets.

Table 7: Possible correspondence of shock ages of OCs and family-formation events.

shock	family	
My	–	
100	Agnia (H)	
400	Merxia (H)	
900	Phocaea (H)	
3600	Maria (H)	if older
3900	Koronis (H)	if older
470	Massalia (L)	if younger
470	Gefion (L)	if younger
470	Juno (L)	if younger
500?	Nysa (LL)	
1000?	Flora (LL)	
4200	Eunomia (LL)	

Table 8: Possible correspondence of cosmic-ray exposure ages of OCs and recent family-formation events.

exposure	family
My	–
6	Karin (H)
8	Koronis$_{(2)}$ (H)
20?	Karin series (H)?
30?	Karin series (H)?
40?	Massalia$_{(2)}$ (L)?
15?	? (LL)

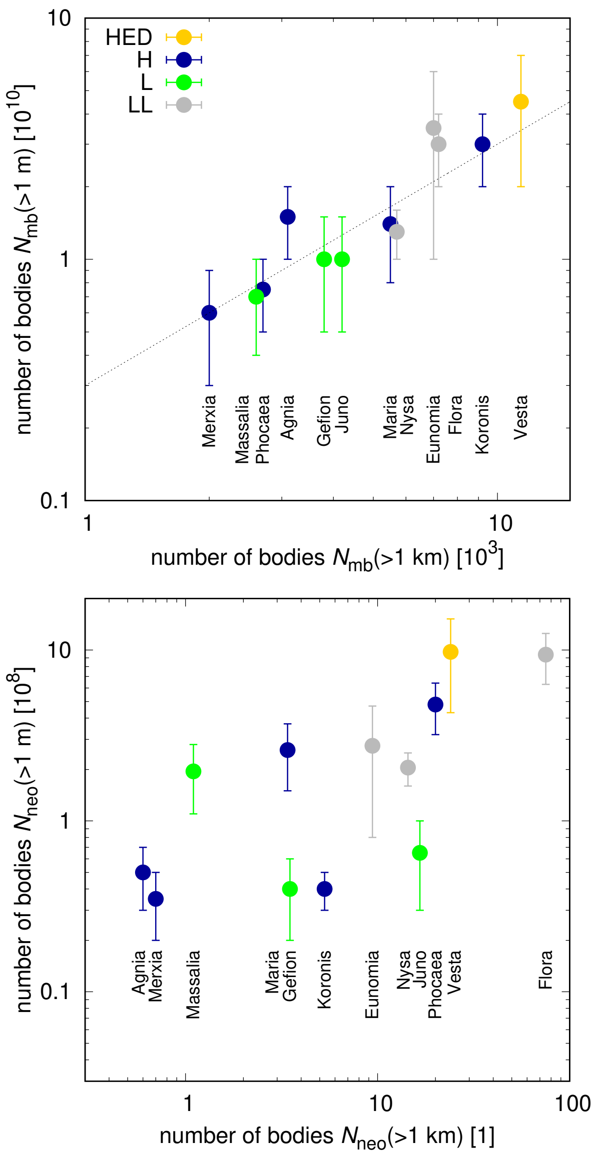

Figure 5: **Illustration of the so-called 'NEO–meteorite conundrum' [20].** The Flora family, identified via previous surveys as the main source of kilometre-sized NEOs, which we confirm here, should also be the most productive in terms of meteoroids along with the Vesta family. Yet, it is not what meteorite fall statistics tell us. Top: The numbers of bodies $N_{\rm mb}(>1\,{\rm km})$ and $N_{\rm mb}(>1\,{\rm m})$ in the main belt, which exhibits a positive correlation. Bottom: The same for the NEO population originating from these families. Individual families have been compositionally linked to meteorite classes (H, L, LL; indicated by colours). The number of H- or L-chondrites never exceeds that of LL-chondrites, which is in contradiction with meteorite fall statistics (H 40%, L 46%, LL 8%; [37]).

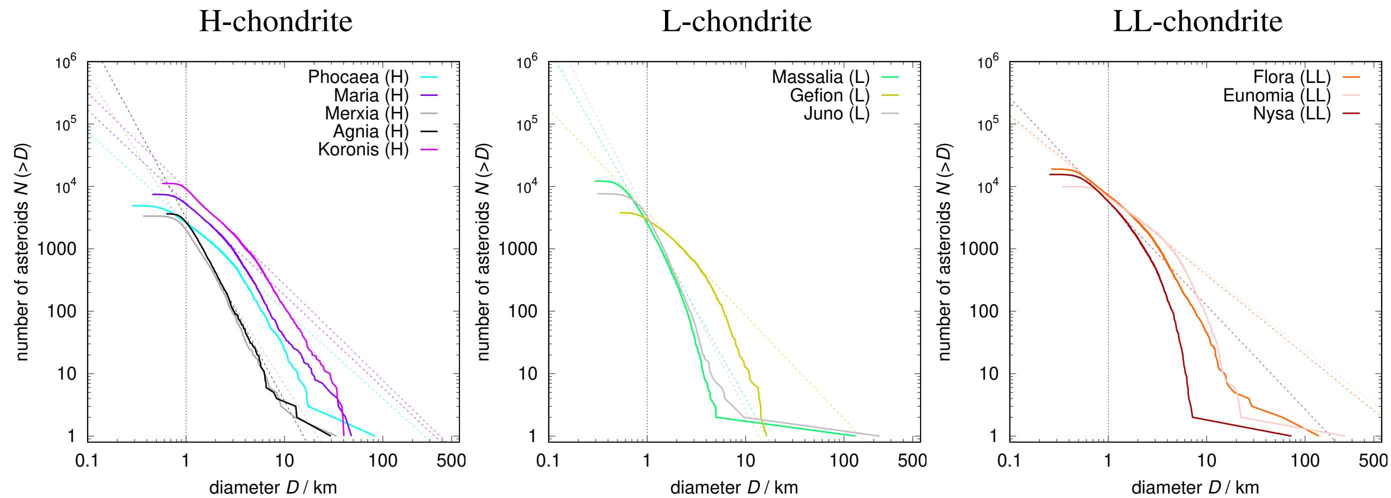

Figure 6: Observed cumulative size-frequency distributions (SFDs) of the S-type asteroid families: H-chondrite-like (left), L-chondrite-like (middle), and LL-chondrite-like (right). Each group is dominated by one or two families, but it sensitively depends on the respective diameter D. For reference, $D = 1\,\mathrm{km}$ is indicated (black dotted line). The SFDs exhibit the following features: largest remnant (LR), possibly an intermediate-size fragment, largest fragment (LF), first slope (q_1), which is steep, starting at the LF, second slope (q_2), which is shallow, related to long-term collisional evolution, third slope (q_3), which is even shallower, related to the scaling law and observed break in the main belt SFD, fourth slope (q_4) or bend-off, related to observational incompleteness.

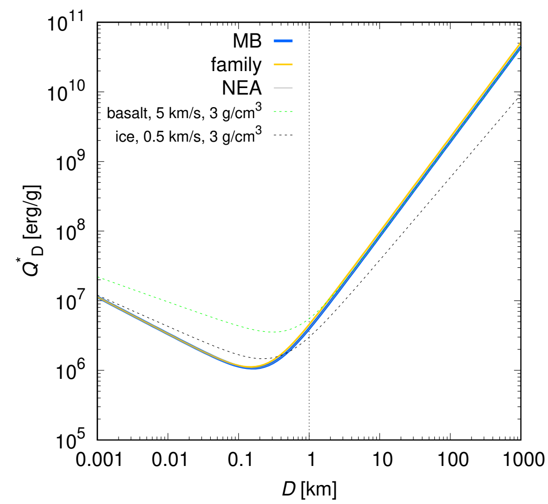

Figure 7: Modified scaling law $Q^{\star}(D)$ used in our collisional model. A comparison to the nominal scaling law for basalt at $5\,\mathrm{km/s}$ (green line) from [58] is also plotted. This modification is needed to fit the main belt SFD at sub-km sizes.

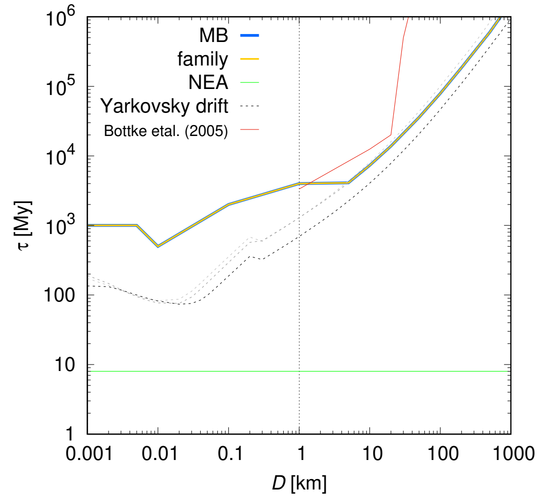

Figure 8: Dynamical decay time scales $\tau(D)$ used in our collisional model. The main belt and families have relatively long time scales, which are needed to fit the NEO population, being transported from the main belt and having a short time scale ($8\,\mathrm{My}$). A comparison to the nominal time scale (red line) of [82] is also plotted. For the Yarkovsky drift without spin axis evolution, decay would be significantly shorter.

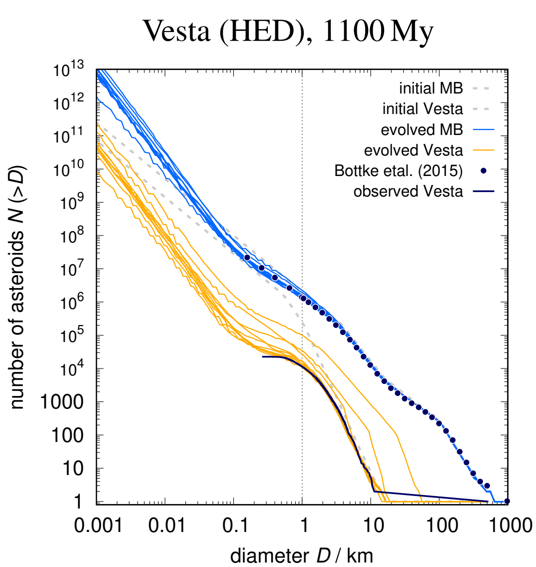

Figure 9: Synthetic SFD of the main belt and the Vesta family, used for calibration. The age $1100 \pm 100\,\mathrm{My}$ is consistent with [63].

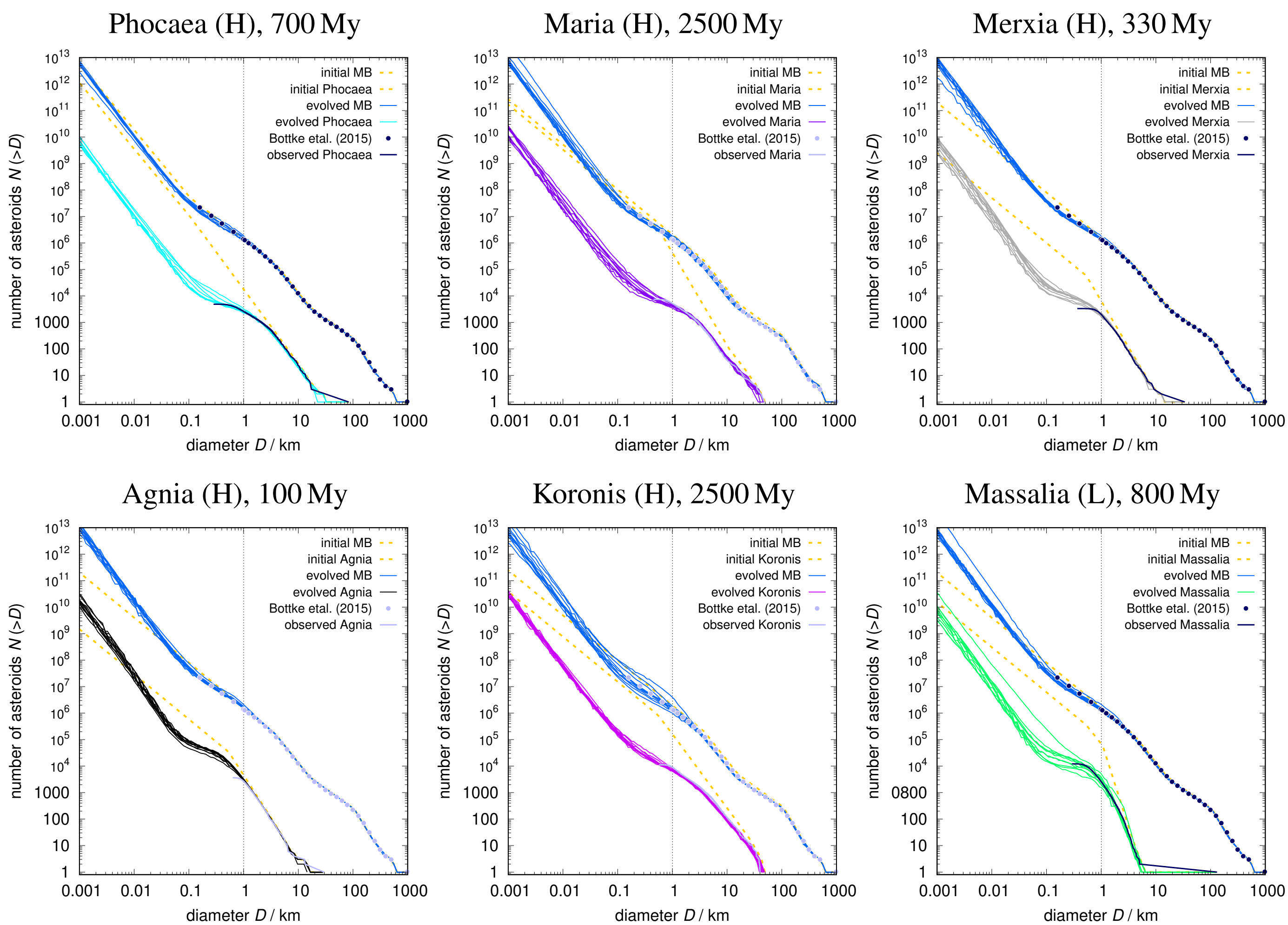

Figure 10: Synthetic SFDs of the S-type asteroid families derived from our collisional model. Every panel contains: the initial main belt, the initial family (yellow dotted), evolved main belt (blue), evolved family (different colours), observed main belt [45], observed family (gray solid). The SFDs between 1 and 10 km were initially a smooth power-law. They evolved due to collisions and exhibit a characteristic slope change at about 5 km, which is observed (see Tab. 1). Every model was run 10 times to account for stochasticity. The best-fit age is reported on top (see Tab. 2).

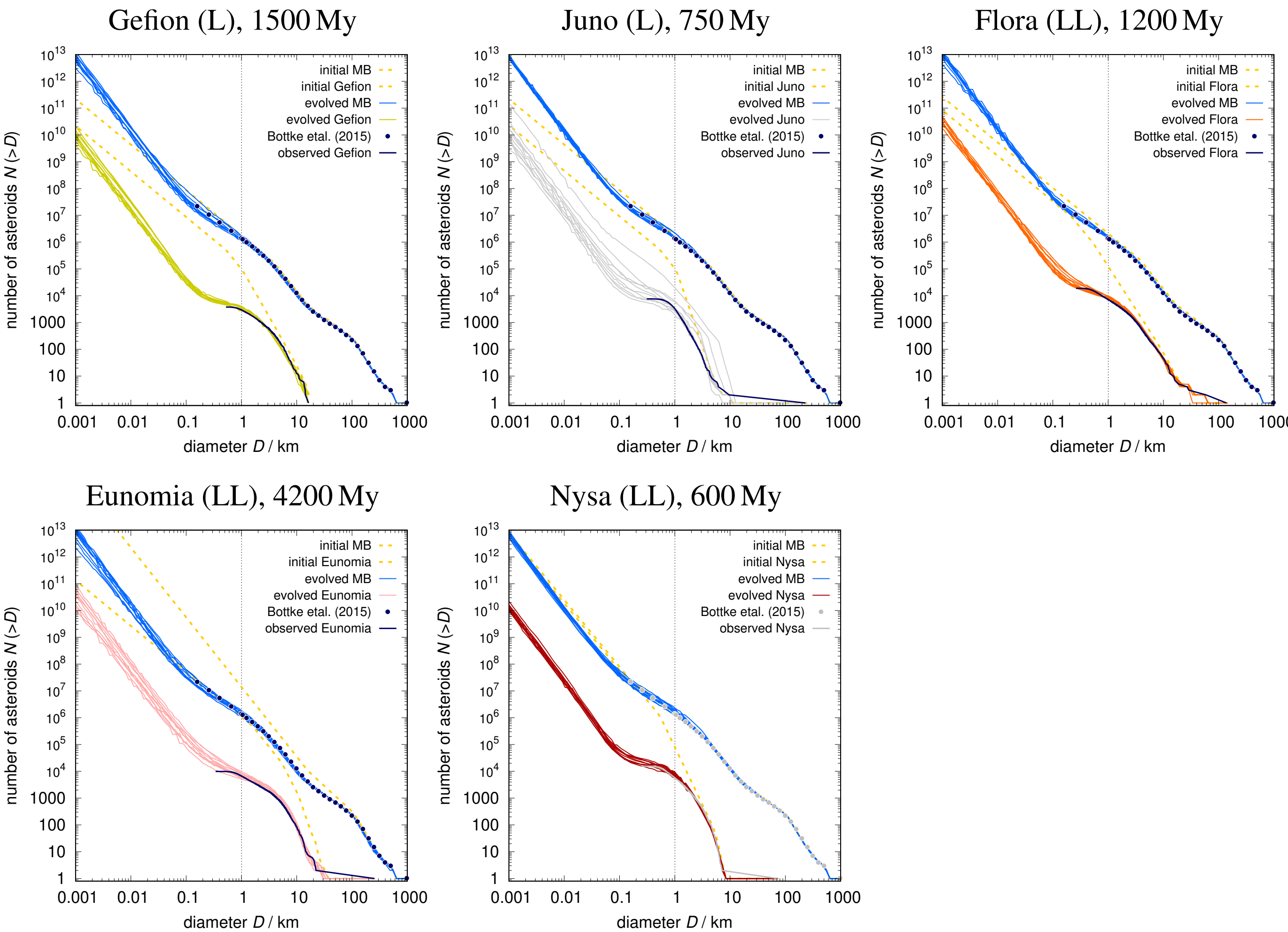

Figure 10: continued.

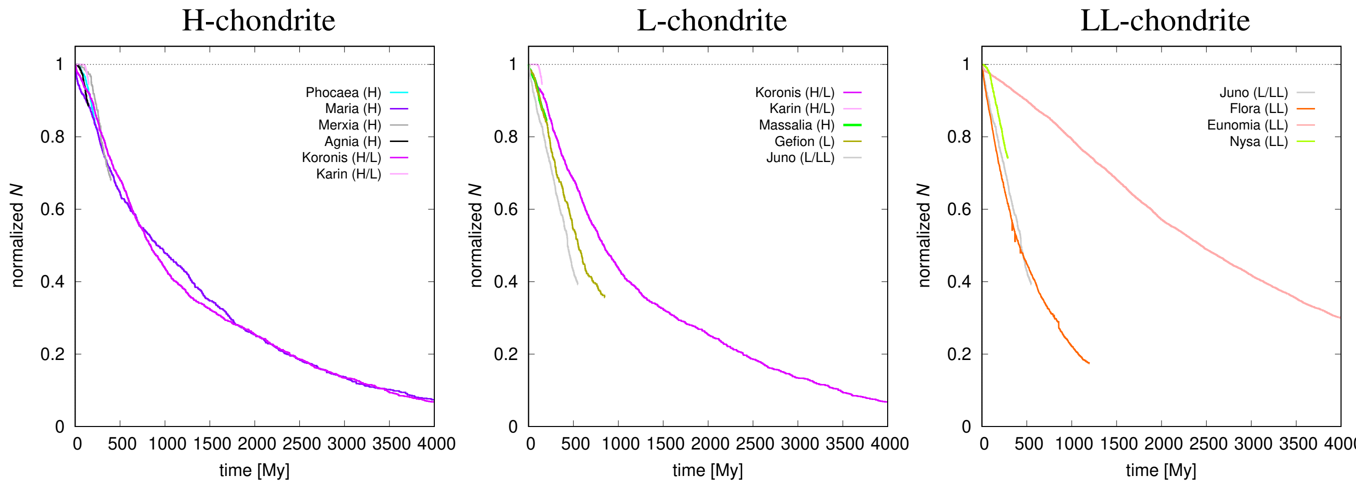

Figure 11: Dynamical decay of selected synthetic asteroid families derived from our orbital model: H-chondrite-like (left), L-chondrite (middle), LL-chondrite (right). Normalized number of bodies vs. time is plotted. The decay is induced by gravitational resonances, the Yarkovsky drift, as modified by the YORP effect, collisional reorientations, and limited by the critical frequency. Sizes of bodies correspond to the observed SFDs; most of them are kilometre-sized.

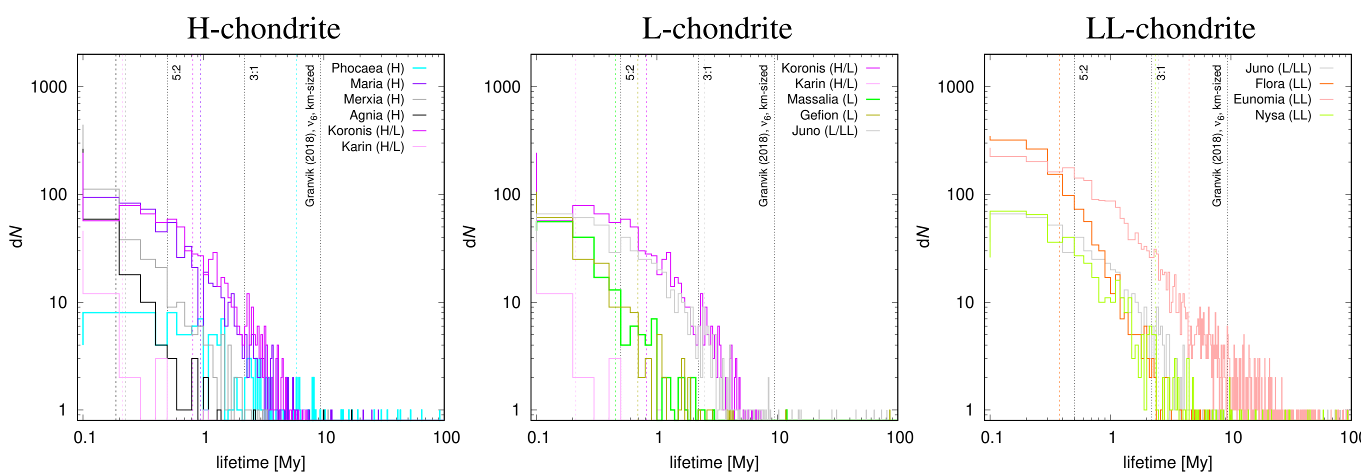

Figure 12: Lifetimes of bodies in the NEO space derived from our orbital model: H-chondrite-like (left), L-chondrite (middle), LL-chondrite (right). When bodies escape from the respective families via resonances (cf. Fig. 19), they temporarily enter the NEO space. Their lifetimes are different for different resonances, where low-order or outer-main-belt ones tend to produce short-lived orbits, and *vice versa*. The mean (*not* median) lifetimes are plotted for each family (colour dashed). For comparison, the lifetimes from [17] (9.4, 2.2, 0.5 My for the ν_6, 3:1, 5:2 resonances; see their Tab. 3) are also plotted (black dotted).

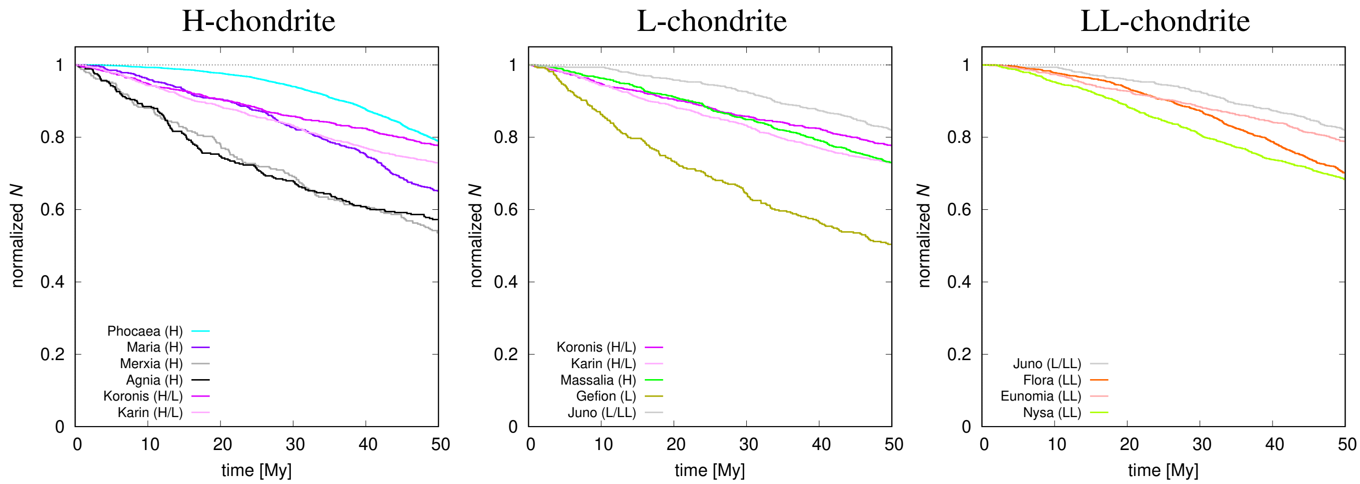

Figure 13: Same as Fig. 11, but for metre-sized bodies.

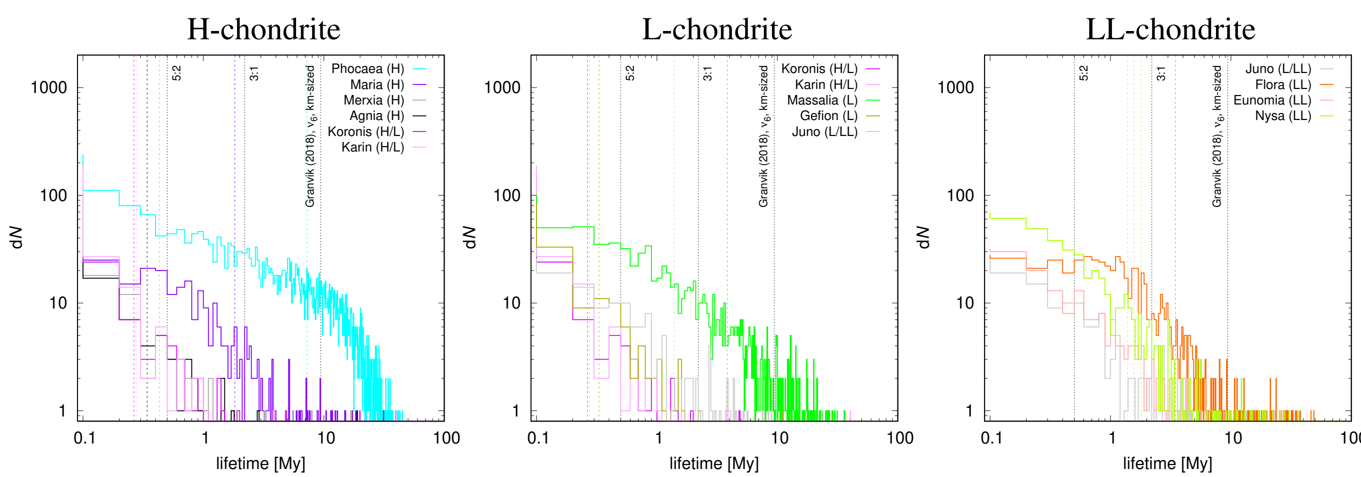

Figure 14: Same as Fig. 12, but for metre-sized bodies.

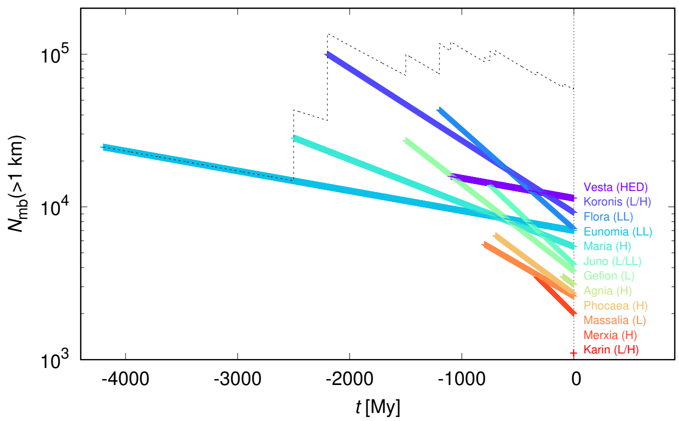

Figure 15: Extrapolated contributions of asteroid families to the population of kilometre-sized bodies in the main belt. The observed number $N_{\rm mb}(>1\,{\rm km})$ is on the right ($t = 0$). Here we account for the dynamical decay only (see Tab. 4; column $\tau_{\rm mb}$), so that at the family origin ($t = t_0$) the population was large and decayed as $\exp(-(t-t_0)/\tau_{\rm mb})$. The total of all selected families is indicated (dashed line). The total of all main belt bodies is 1.36×10^6.

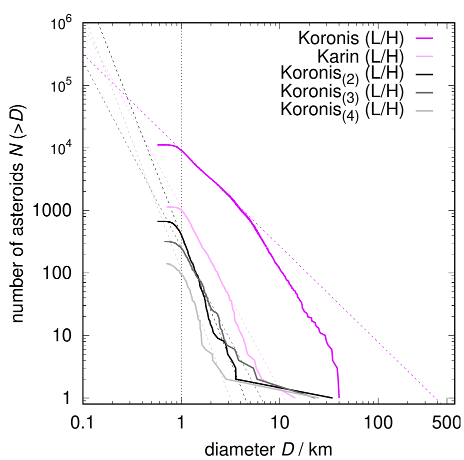

Figure 16: Same as Fig. 6 for the Karin, Koronis$_{(2)}$, Koronis$_{(3)}$, Koronis$_{(4)}$ families.

A Parameters of the principal bodies

Hereinafter, we discuss preferred values of parameters for the largest member of the studied families. (4) Vesta has a volume-equivalent diameter 525 km and a volumetric density $3.456\,\mathrm{g\,cm^{-3}}$ [83]; the parent body size is practically the same as Vesta.

(20) Massalia is 132 km in diameter [50] and its density is $3.71\,\mathrm{g\,cm^{-3}}$ [84], although with a 20% uncertainty.

For (170) Maria, (808) Merxia, (847) Agnia, (158) Koronis, (1272) Gefion, we used diameters 35 km, 33 km, 30 km, 34 km [50], and only 6.9 km [49], even though Gefion is not the largest remnant, it has the lowest designation. Because the densities are unknown, we assumed $3\,\mathrm{g\,cm^{-3}}$. All of these breakups were catastrophic disruptions; parent body size is substantially larger, i.e., 125 km, 50 km, 52 km, 161 km, and 72 km, respectively. This is important for the velocity field. We determined these values by scaling of synthetic SFDs of [85]; uncertainties are of the order of 10 %

(832) Karin is 14.3 km in diameter [50], and the family parent body size is up to 36 km.

For (3) Juno, we used 254 km, $3.15\,\mathrm{g\,cm^{-3}}$, according to [86]. It is the 2nd largest S-type asteroid.

For (8) Flora, 146 km, $2.43\,\mathrm{g\,cm^{-3}}$ from the same reference. If about half of the family members has been lost in the ν_6 resonance the parent body size might have been larger.

(15) Eunomia is 256 km in diameter, and its density $2.96\,\mathrm{g\,cm^{-3}}$ is close the mean density of S-types [50,86]. It is the 1st largest S-type asteroid.

Finally, (44) Nysa is E-type, (135) Hertha is M-type; both are likely interlopers in the respective S-type family. Even without these interlopers, the parent-body size is up to about 80 km, as determined by the [85] method.

B Family ages

Previous orbital modelling, cratering record, or meteorite radiometry can be used to estimate the age of an asteroid family. The Vesta family is constrained by the Rheasylvia basin on Vesta, or *in* *situ* observations [63,64], as $(1000 \pm 200)\,\mathrm{My}$. It is in agreement with our collisional model (Tab. 2).

The Phocaea family was studied by [87]; it is up to 2200 My old, as inferred from the Yarkovsky drift rates. Its SFD indicates a younger age (cf. Tab. 2).

The Massalia family is $(152 \pm 18)\,\mathrm{My}$ old according to [53]. Parameters of the velocity field were also estimated, $v_5 = 24\,\mathrm{m\,s^{-1}}$, $D_5 = 5\,\mathrm{km}$, $v \propto D^{-1}$. On contrary, its shallow SFD indicates an older age.

The Maria family may be up to $3000 \pm 1000\,\mathrm{My}$ old, according to (a_p, H) distribution [88].

The Merxia family, $(330 \pm 50)\,\mathrm{My}$ old [53], is almost certainly young, having a smooth and steep SFD from the LR to the observational incompleteness.

The Agnia family is $(100 \pm 25)\,\mathrm{My}$ old [55], again smooth and steep.

On contrary, the Koronis family is really old, $(2500 \pm 1000)\,\mathrm{My}$ [88]. Koronis is probably even older than Maria, because the 'break' of the SFD is at larger D's (3 vs. 5 km).

The Gefion family is constrained by radiometry of LL chondrites $(467 \pm 2)\,\mathrm{My}$ [67,89], and compatible with the Yarkovsky/YORP model. On contrary, its SFD is shallow, which indicates an older age.

For the Juno family, we assume $(750 \pm 150)\,\mathrm{My}$, according to [90].

The Flora family was estimated to be $(1200 \pm 200)\,\mathrm{My}$ old [91]. Our N-body modelling suggests that the synthetic family should be more extended, with a substantially larger $D_\mathrm{PB} > 146\,\mathrm{km}$. About half of bodies was lost in the ν_6 resonance.

The Eunomia family is probably $(3200 \pm 1000)\,\mathrm{My}$ old [90]. Our N-nody modelling suggests a range 1880 up to $3300\,\mathrm{My}$ on the basis of the $(a_\mathrm{p}, e_\mathrm{p})$ distribution. It almost reaches a steady state, because we recalibrate the synthetic SFD to the observed SFD in every time step, which is then insensitive to the decay of the population [72]. Eunomia is most likely older than Flora (cf. the 'break').

Finally, the Nysa family is difficult to distinguish from other overlapping families in the same

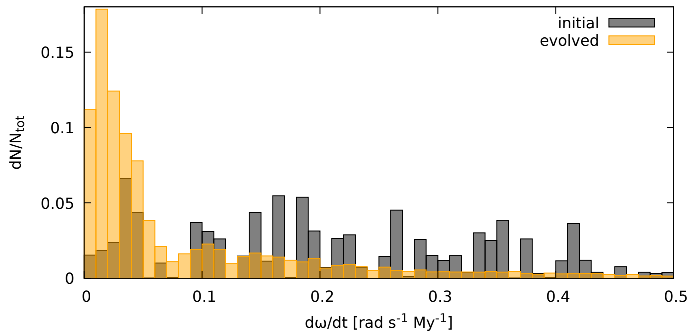

Figure 17: Normalized differential distribution $\mathrm{d}N/N_{\mathrm{tot}}$ of spin accelerations $\mathrm{d}\omega/\mathrm{d}t$ (in $\mathrm{rad\,s^{-1}\,My^{-1}}$) for a population of metre-sizes bodies originated from the Agnia family; close to the initial conditions (black) and evolved due to the YORP effect (orange). A strong preference for 'slow' shapes is evident.

region [56]. S-type bodies are clustered around (135) Hertha and the upper limit of its age is $350\,\mathrm{My}$ [92].

C Selection of 'slow' shapes.

In our orbital model, we noted a strong dynamical selection of shapes, which evolve slowly due to the YORP torque (Fig. 17). If the shape is 'fast', the critical rotation frequency is reached fast, this shape is changed to another one, and *vice versa*.

Out of 200 nominal shapes from [36], e.g., 185, 101, 129, 106, 58, ... are slow (see Fig. 18). They seem to be more round, but it is generally difficult to recognize it. They should be less like a wind-mill [93].

Moreover, the scaling relation we use in our model:

$$c = c_{\mathrm{YORP}} \left(\frac{a}{a_0}\right)^{-2} \left(\frac{R}{R_0}\right)^{-2} \left(\frac{\rho}{\rho_0}\right)^{-1}, \qquad (12)$$

where $a_0 = 2.5\,\mathrm{au}$, $R_0 = 1\,\mathrm{km}$, $\rho_0 = 2.5\,\mathrm{g\,cm^{-3}}$, is not complete. A scaling with the rotation period (or frequency) is missing. While the nominal period $P_0 = 6\,\mathrm{h}$, for which the torques were originally computed, is too long for meteoroids, the YORP effect should work even in the limit of zero conductivity [93]. It implies a negligible dependence on the rotation period. This may change, if a transversal heat diffusion in mm- to cm-scale surface features is properly taken into account [94,95]. However, it would require a dedicated computation of the YORP effect for metre-sized bodies.

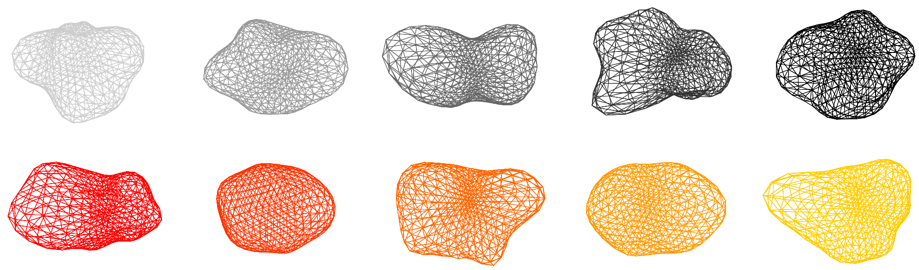

Figure 18: Examples of shapes from [36], which exhibit fast (top) vs. slow (bottom) evolution of the spin rate due to the YORP effect. The latter appear to be more round, but it is generally difficult to recognize a shape exhibiting a large vs. small YORP torque.

D Supplementary tables

The intrinsic collisional probability and the mean collisional velocity were computed with [96] theory for precessing orbits. The values for various combinations of populations are listed in Tabs. 9, 10. The flux of meteoroids originating from families, accounting for various collisional probabilities with the Earth, is listed in Tab. 11.

Table 9: Intrinsic collisional probability and the mean collisional velocity for various main belt populations.

populations	p	v
–	$10^{-18}\,\mathrm{km}^{-2}\,\mathrm{y}^{-1}$	$\mathrm{km\,s}^{-1}$
MB–MB	2.860	5.772
MB–Agnia	4.466	4.471
MB–Eunomia	3.347	5.784
MB–Flora	2.736	5.667
MB–Gefion	3.545	5.115
MB–Juno	3.009	6.491
MB–Koronis	4.657	4.271
MB–Maria	2.923	6.095
MB–Massalia	4.269	5.042
MB–Merxia	4.057	4.744
MB–Nysa	3.986	5.093
MB–Phocaea	2.419	8.252
MB–Vesta	2.919	5.288
Agnia–Agnia	10.535	2.241
Eunomia–Eunomia	5.961	5.725
Flora–Flora	15.506	4.235
Gefion–Gefion	5.913	4.352
Juno–Juno	4.950	7.034
Karin–Karin	14.865	1.531
Koronis–Koronis	13.323	1.625
Maria–Maria	7.112	5.866
Massalia–Massalia	29.009	4.234
Merxia–Merxia	8.235	3.571
Nysa–Nysa	20.324	4.766
Phocaea–Phocaea	5.936	10.307
Vesta–Vesta	12.601	3.613

Table 10: Same as Tab. 9 for the Earth and meteoroids in the NEO space.

populations	p	v
–	$10^{-18}\,\mathrm{km}^{-2}\,\mathrm{y}^{-1}$	$\mathrm{km}\,\mathrm{s}^{-1}$
Earth–Agnia	120.524	24.672
Earth–Eunomia	46.952	24.992
Earth–Flora	44.860	21.663
Earth–Gefion	123.191	21.484
Earth–Juno	47.467	23.907
Earth–Karin	76.386	25.567
Earth–Koronis	115.815	19.872
Earth–Maria	49.847	27.295
Earth–Massalia	78.412	22.851
Earth–Merxia	43.796	19.474
Earth–Nysa	77.398	21.787
Earth–Phocaea	9.306	31.419
Earth–Vesta	49.352	22.963

Table 11: Meteoroid flux $\Phi = pN_{\rm neo}$.

family	Φ
–	$10^{-9}\,\mathrm{km}^{-2}\,\mathrm{y}^{-1}$
Vesta (HED)	21.5-75.1
Phocaea (H)	3.0-5.9
Maria (H)	7.4-18.5
Merxia (H)	0.7-2.1
Agnia (H)	4.0-8.0
Koronis (H)	3.0-6.0
Karin (H)	29.6-59.3
Massalia (L)	8.6-21.6
Gefion (L)	2.6-7.9
Juno (L)	1.6-4.8
Flora (LL)	28.1-56.3
Eunomia (LL)	3.7-22.1
Nysa (LL)	12.2-19.4
HED	21.5-75.1
H	47.7-99.8
L	12.8-34.3
LL	44.0-97.8
H+L+LL	104.5-231.9
all bodies	3900^{C}
with 2nd Koronis:	
$\mathrm{Koronis}_{(2)}$	98.8-296.4
H	146.5-396.2
with 2nd Massalia:	
$\mathrm{Massalia}_{(2)}$	216.1-648.2
L	228.9-682.5

Notes. ^{C} 41

E Supplementary figures

We show the outcome of families identification procedure and a preferred extent of the families in Fig. 19, and pre-atmoshperic orbits of H chondrites in Fig. 20.

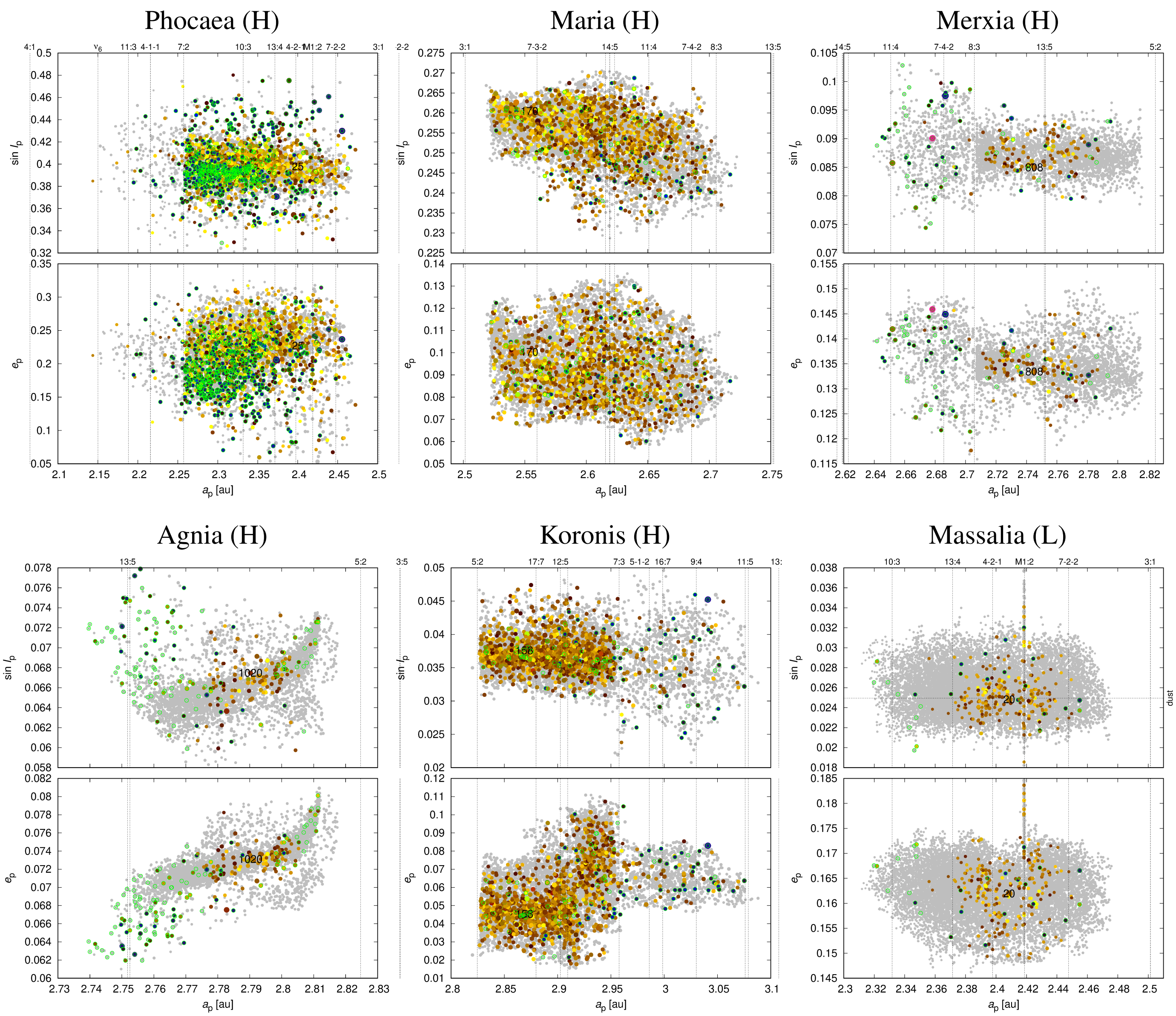

Figure 19: S-type families as identified in this work. The proper semimajor axis $a_{\rm p}$ vs. the proper eccentricity $e_{\rm p}$ and vs. the proper inclination $\sin I_{\rm p}$ are plotted. Colours correspond to the geometric albedo $p_{\rm V}$ (blue $\rightarrow$ yellow for C- to S-type). Major mean-motion and three-body resonances (vertical dotted lines), as well as identified interlopers (green circles) are indicated. Some of the bodies ((20) Massalia, (832) Karin) have inclinations corresponding to the IRAS dust bands (horizontal dotted lines).

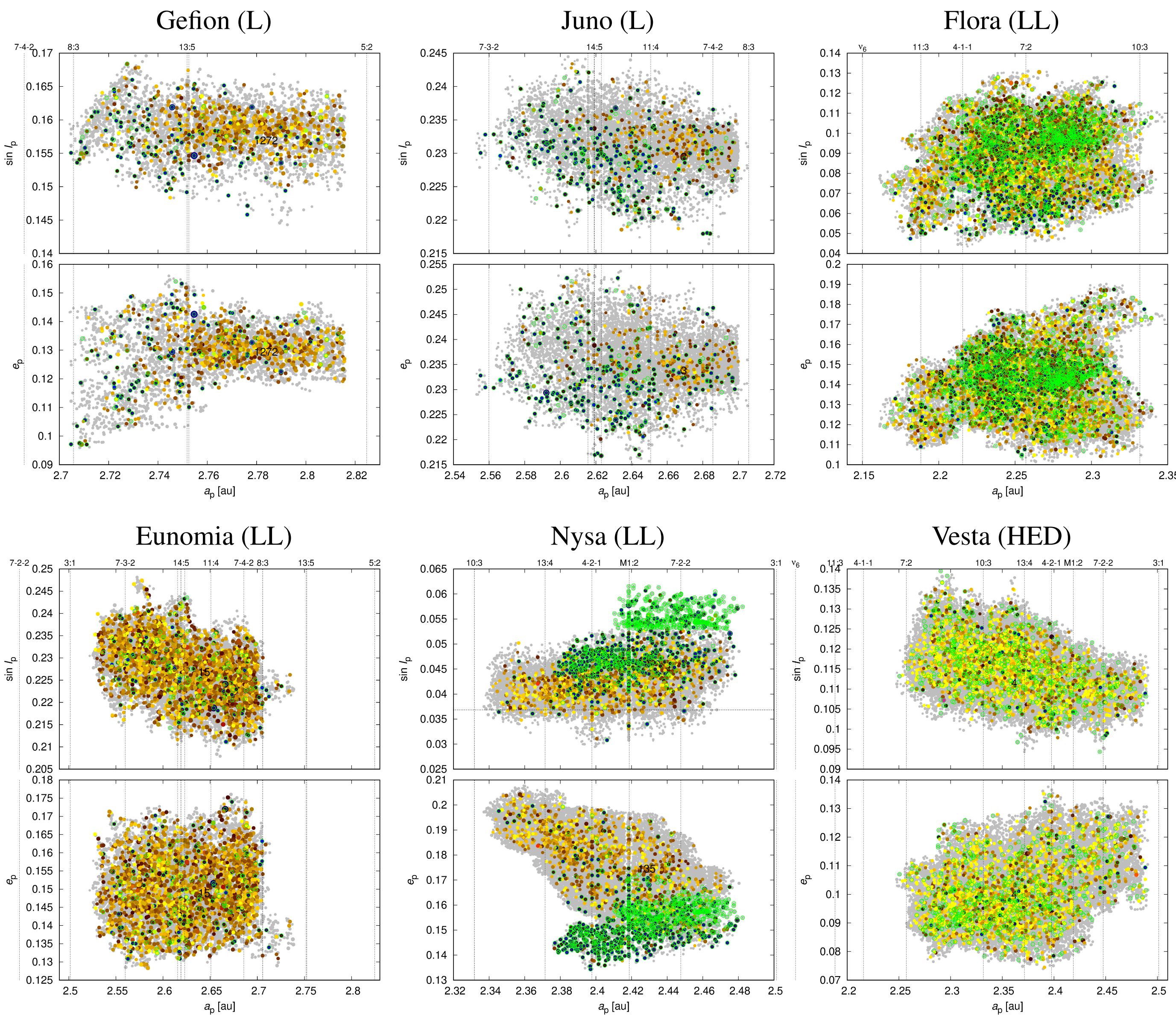

Figure 19: continued.

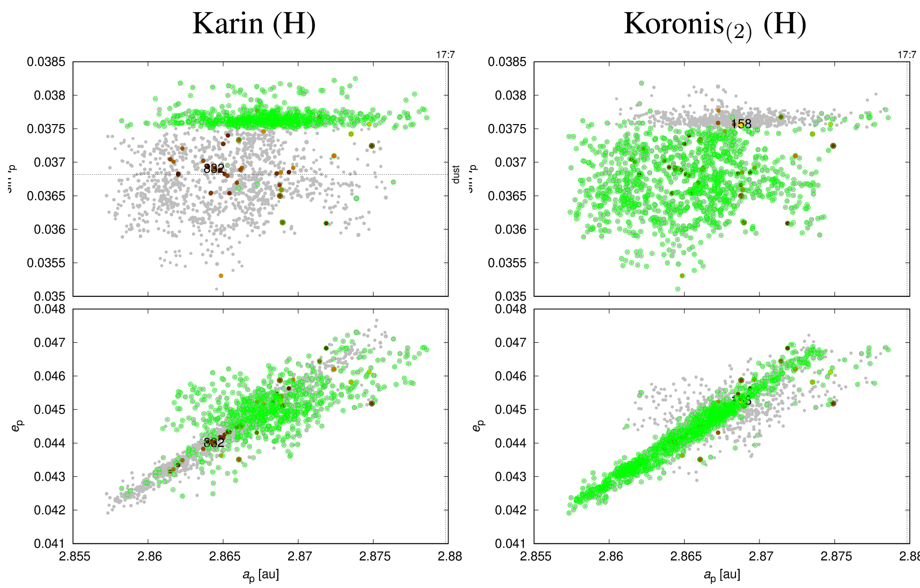

Figure 19: continued.

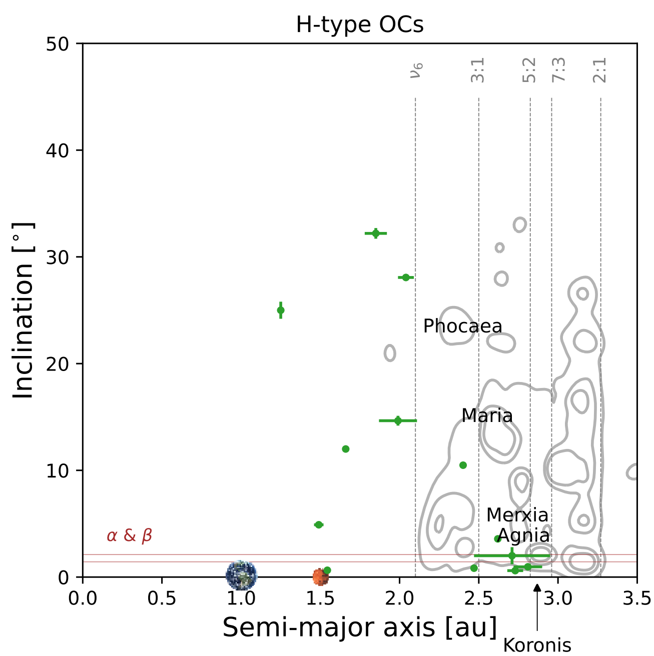

Figure 20: Pre-atmospheric orbital elements of 14 H-chondrite falls. The osculating semimajor axis versus the inclination are plotted with their uncertainties (error bars). Some H chondrites have the semimajor axis 2.5-2.8 au and low inclination ($\lesssim 3°$), which corresponds to the Koronis family, whereas other orbits were scattered by close encounters with terrestrial planets. Data from [38]; `https://www.meteoriteorbits.info/`.